A STEEPER THAN LINEAR DISK MASS–STELLAR MASS SCALING RELATION

I. Pascucci[1,12], L. Testi[2,3,13], G. J. Herczeg[4], F. Long[4], C. F. Manara[5], N. Hendler[1], G. D. Mulders[1,12], S. Krijt[6,12], F. Ciesla[6,12], Th. Henning[7], S. Mohanty[8], E. Drabek-Maunder[8], D. Apai[1,9,12], L. Szűcs[10], G. Sacco[3], AND J. Olofsson[11]

[1] Lunar and Planetary Laboratory, University of Arizona, Tucson, AZ 85721, USA; pascucci@lpl.arizona.edu
[2] European Southern Observatory, Karl-Schwarzschild-Strasse 2, D-85748 Garching bei München, Germany
[3] INAF-Arcetri, Largo E. Fermi 5, I-50125 Firenze, Italy
[4] Kavli Institute for Astronomy and Astrophysics, Peking University, Yi He Yuan Lu 5, Haidian Qu, 100871 Beijing, China
[5] Scientific Support Office, Directorate of Science, European Space Research and Technology Centre (ESA/ESTEC),
Keplerlaan 1, 2201 AZ Noordwijk, The Netherlands
[6] Department of the Geophysical Sciences, University of Chicago, Chicago, IL 60637, USA
[7] Max Planck Institute for Astronomy, Königstuhl 17, D-69117 Heidelberg, Germany
[8] Imperial College London, 1010 Blackett Lab, Prince Consort Road, London SW7 2AZ, UK
[9] Steward Observatory, University of Arizona, Tucson, AZ 85721, USA
[10] Max-Planck-Institut für extraterrestrische Physik, Giessenbachstrasse 1, D-85748 Garching, Germany
[11] Instituto de Fisica y Astronomia, Facultad de Ciencias, Universidad de Valparaiso, Playa Ancha, Valparaiso, Chile

ABSTRACT

The disk mass is among the most important input parameter for every planet formation model to determine the number and masses of the planets that can form. We present an ALMA 887 μm survey of the disk population around objects from ∼2 to 0.03 $M_{\odot}$ in the nearby ∼2 Myr old Chamaeleon I star-forming region. We detect thermal dust emission from 66 out of 93 disks, spatially resolve 34 of them, and identify two disks with large dust cavities of about 45 au in radius. Assuming isothermal and optically thin emission, we convert the 887 μm flux densities into dust disk masses, hereafter $M_{\rm dust}$. We find that the $M_{\rm dust}$–M_{*} relation is steeper than linear and of the form $M_{\rm dust} \propto (M_{*})^{1.3-1.9}$, where the range in the power-law index reflects two extremes of the possible relation between the average dust temperature and stellar luminosity. By reanalyzing all millimeter data available for nearby regions in a self-consistent way, we show that the 1–3 Myr old regions of Taurus, Lupus, and Chamaeleon I share the same $M_{\rm dust}$–M_{*} relation, while the 10 Myr old Upper Sco association has a steeper relation. Theoretical models of grain growth, drift, and fragmentation reproduce this trend and suggest that disks are in the fragmentation-limited regime. In this regime millimeter grains will be located closer in around lower-mass stars, a prediction that can be tested with deeper and higher spatial resolution ALMA observations.

Key words: brown dwarfs – protoplanetary disks – stars: pre-main sequence – submillimeter: planetary systems

Supporting material: data behind figure, extended figures, machine-readable tables

1. INTRODUCTION

The number of known exoplanets has grown exponentially in the past decade, revealing systems that are unlike our solar system (e.g., Winn & Fabrycky 2015). While there is clearly a large diversity in planetary architectures, several trends with the mass of the central star are emerging. These include (i) a positive correlation between stellar mass and the occurrence rate of Jovian planets within a few au (e.g., Johnson et al. 2010; Howard et al. 2012; Bonfils et al. 2013), although no correlation is present for the population of hot Jupiters within a 10-day period (Obermeier et al. 2016); and (ii) a larger occurrence rate of close-in Earth-sized planets around M dwarfs than around Sun-like stars (Dressing & Charbonneau 2013; Mulders et al. 2015a). These trends are likely the result of stellar-mass-dependent disk properties. Indeed, planet formation models find that the disk mass strongly impacts the frequency and location of planets that can form, from giants down to Earth-sized planets (e.g., Raymond et al. 2007; Alibert et al. 2011; Mordasini et al. 2012). Therefore, the scaling of

disk mass versus stellar mass will yield a stellar mass dependence for the planet population.

Measuring gas disk masses is notoriously challenging both in the early (∼1–10 Myr) protoplanetary phase (e.g., Kamp et al. 2011; Miotello et al. 2014) and in the late debris disk phase (e.g., Pascucci et al. 2006; Moór et al. 2015). The disk mass in solids, up to millimeter–centimeter in size, is better constrained via continuum millimeter- to centimeter-wavelength observations since the emission from most dust grains is optically thin at these wavelengths. Still, individual dust disk masses can have an order-of-magnitude uncertainty because the absolute value of the dust opacity, which depends on both the grain composition and size distribution, is not known (e.g., Beckwith et al. 2000).

Pre-ALMA millimeter surveys of nearby star-forming regions provided dust disk masses for over 100 young stars, primarily with K and early M spectral types (see Williams & Cieza 2011; Testi et al. 2014 for reviews). In spite of a large scatter in disk masses at any stellar mass, the data were consistent with a linear disk mass ($M_{\rm dust}$)–stellar mass (M_{*}) scaling relation (Andrews et al. 2013; Mohanty et al. 2013), as hinted earlier on by the detection of a few bright disks around substellar objects (Klein et al. 2003; Scholz et al. 2006; Harvey et al. 2012). However, these studies were dominated by upper limits below the M0 spectral type, meaning that they only probed the upper envelope of disk masses in the low stellar

---

mass end. This left open the possibility of a steeper M_{dust}–M_* relation buried in the nondetections. This suspicion was corroborated by the observation that stellar accretion rates ($\dot{M}$), tracing the gas disk component, display a steeper dependence with stellar mass when the population of low-mass stars is well sampled (e.g., Natta et al. 2006; Fang et al. 2009; Rigliaco et al. 2011; Alcalá et al. 2014). If the steeper relation is due to the way disks viscously evolve and disperse (e.g., Alexander & Armitage 2006; Hartmann et al. 2006; Ercolano et al. 2014) and if M_{dust} somehow traces the total (gas +dust) disk mass, $\dot{M}$ and M_{dust} should scale similarly with stellar mass.

The increased sensitivity of ALMA is now enabling us to survey entire star-forming regions and to probe the millimeter luminosity of young (∼1–10 Myr) protoplanetary disks identified in previous infrared images. The 1.3 mm survey of the Orion OMC1 detected continuum emission toward 49 cluster members and reported no correlation between M_{dust} and M_* (Eisner et al. 2016). However, as also pointed out by the authors, the statistical significance of this result is limited given the small number of ALMA detections and that spectroscopically determined stellar masses in the OMC1 are only available for less than half of the ALMA-detected sources. The survey of the 5–10 Myr old Upper Sco association (Slesnick et al. 2008) covered all known disks around stars from ∼0.15 to 1.5 $M_\odot$ and reported a steeper than linear relation between M_{dust} and M_* (Barenfeld et al. 2016). After removing debris/evolved transitional disks, they also found that the M_{dust}/M_* ratio in Upper Sco is ∼4.5 times lower than that in Taurus, suggesting that significant evolution occurs in the outer disk between 1 and 10 Myr. Finally, Ansdell et al. (2016) carried out a similarly sensitive ALMA survey in the much younger (∼1–3 Myr) Lupus star-forming clouds, covering sources in the I–IV regions, which most likely trace different stages of disk evolution. One of the main results of the Ansdell et al. (2016) survey is that the M_{dust}–M_* relation in Lupus is similar to that in Taurus and shallower than that in Upper Sco.

Here we present an ALMA 887 μm survey of the ∼2 Myr old Chamaeleon I star-forming region targeting disks around objects ranging from $2 M_\odot$ down to the substellar regime (Sections 2 and 3). We demonstrate that the M_{dust}–M_* relation in Chamaeleon I is steeper than linear, under a broad range of assumptions made to convert flux densities into dust disk masses (Sections 4 and 5). By reanalyzing in a self-consistent way all the submillimeter fluxes and stellar properties available for other nearby star-forming regions, we also show that Taurus, Lupus, and Chamaeleon I have the same M_{dust}–M_* relation, within the inferred uncertainties, and confirm that the one in Upper Sco is steeper (Section 6). We discuss the possibility that the steeper relation traces either the growth of pebbles into larger solids that become undetectable by ALMA or a more efficient inward drift in disks around the lowest-mass stars (Section 6).

2. THE CHAMAELEON I SAMPLE

In previous studies our group has assembled the stellar properties and spectral energy distribution (SED) of each Chamaeleon I member and used continuum radiative transfer codes to model disk structures down to the substellar regime (Szűcs et al. 2010; Mulders & Dominik 2012; Olofsson et al. 2013). Our modeling included optical, Two Micron All Sky

Survey (2MASS), *Spitzer*, *WISE*, and, when available, *Herschel* and millimeter photometry. We did not include any spectroscopic data, e.g., *Spitzer* IRS spectra. Only objects displaying excess emission at more than one wavelength were included in our ALMA survey. In this way we excluded all Class III objects (Luhman et al. 2008). In addition, we removed the few known Class 0 and I sources (Luhman et al. 2008; Belloche et al. 2011). These criteria result in 93 objects with dust disks, mostly Class II, but see later for subgroups. Table 1 includes their 2MASS designations, other commonly used names, multiplicity information from the literature, and the spectral types from Luhman (2007, 2008). The latter information was also used to set the exposure times (see Section 3). We note that our sample is not complete in the substellar regime (spectral type later than M6). For instance, the well-known disk around the M7.75 brown dwarf Cha Hα1 (e.g., Pascucci et al. 2009) is not included in our ALMA survey. Our ALMA sample also includes 32 known multiple stars. Assuming an average distance of 160 pc to the Chamaeleon I star-forming region (Luhman 2008), 7/32 are "close" binaries, with projected separations ≤40 au that are small enough to affect disk evolution (Kraus et al. 2012).

The SEDs of 87 of our ALMA targets are classified in Luhman et al. (2008) and Manoj et al. (2011) using the spectral slope $\alpha = d \log(\lambda F_\lambda)/d \log \lambda$ between ∼2 μm (2MASS K-band photometry) and 24 μm (*Spitzer*/MIPS photometry in the first contribution and *Spitzer*/IRS spectroscopy in the second). As discussed in Manoj et al. (2011), the two SED classifications are in good agreement. Six of our ALMA targets[14] were not observed with *Spitzer*, but all have WISE photometry at 12 μm (W3 channel; Cutri et al. 2012). We use the following approach to classify them. First, we plot the de-reddened[15] α_{2-24} versus α_{2-12} for all Chamaeleon I members that have 2MASS K-band, WISE 12 μm, and MIPS 24 μm photometry. From this plot we find that the two quantities are well correlated and the best-fit relationship is $\alpha_{2-24} = 1.14(\pm0.03) \times \alpha_{2-12} + 0.38(\pm0.06)$. Hence, we use this relationship to compute α_{2-24} from the measured α_{2-12} for the six unclassified sources. The inferred α_{2-24} spectral indices are between −1.7 and −0.9, all Class II SED following Manoj et al. (2011). The transitional disks (Class II/T) are identified as having a deficit of flux at wavelengths less than 8 μm compared with the Class II median and comparable or higher excess emission beyond ∼13 μm following Kim et al. (2009) and Manoj et al. (2011). By excluding the IRS *Spitzer* spectroscopy from our analysis, we missed the Class II/T disk around the M0 star Sz 18, also known as T25 (Kim et al. 2009). Its infrared excess is only pronounced beyond ∼15 μm, and the source was outside the MIPS 24 μm field of view (Luhman et al. 2008), thus appearing as a Class III source based on the available photometry. In summary, our sample includes 3 flat spectra (FS), 82 Class II, and 8 Class II/T.

As part of a parallel effort to simultaneously derive stellar parameters, extinction, and mass accretion rates, our group has obtained VLT X-Shooter spectra for 89 out of 93 of our ALMA Chamaeleon I targets. The observations, data reduction, and

---

[14] The six unclassified targets are J11160287−7624533, J11085367 −7521359, J10561638−7630530, J11071181−7625501, J11175211 −7629392, and J11004022−7619280.
[15] To de-redden the magnitudes, we used the A_J extinctions provided in Luhman (2007) and the Mathis (1990) reddening law because all of our sources have low extinction, $A_J < 0.8$.

Table 1
Source Properties

2MASS	Other Name	Multiplicity (arcsec)	Ref.	Spectral Type Luhman	SED	ALMA Sample	Spectral Type Adopted	Ref.	$\log(M_*)$ $(M_\odot)$
J10533978−7712338				M2.75	II	Hot	M2	M16b	−0.41[a]
J10555973−7724399	T3	2.210	D13	M0	II	Hot	K7	M16a	−0.13 (−0.17, −0.07)
J10561638−7630530	ESOHα553			M5.6	II	Cool	M6.5	M16b	−0.96 (−1.03, −0.89)
J10563044−7711393	T4			M0.5	II	Hot	K7	M16a	−0.07 (−0.15, 0.19)
J10574219−7659356	T5	0.160	N12	M3.25	II	Hot	M3	M16b	−0.52 (−0.57, −0.47)
J10580597−7711501				M5.25	II	Cool	M5.5	M16b	−0.96 (−1.06, −0.86)
J10581677−7717170	SzCha	5.120	D13	K0	II/T	Hot	K2	M14	0.10 (0.06, 0.14)
J10590108−7722407	TWCha			K2	II	Hot	K7	M16a	−0.07 (−0.14, 0.17)
J10590699−7701404	CRCha			K2	II	Hot	K0	M16a	0.23 (0.18, 0.28)
J11004022−7619280	T10			M3.75	II	Cool	M4	M16b	−0.62 (−0.69, −0.54)
J11022491−7733357	CSCha			K6	II/T	Hot	K2	M14	0.13 (0.09, 0.20)
J11023265−7729129	CHXR71	0.560	D13	M3	II	Hot	M3	M16b	−0.52 (−0.58, −0.45)
J11025504−7721508	T12			M4.5	II	Cool	M4.5	M16a	−0.74 (−1.23, −0.68)
J11040425−7639328	CHSM1715			M4.25	II	Cool	M4.5	M16b	−0.74 (−0.83, −0.65)
J11040909−7627193	CTChaA	2.670	D13	K5	II	Hot	K5	M16a	−0.06 (−0.16, 0.04)
J11044258−7741571	ISO52			M4	II	Cool	M4	M16a	−0.62 (−0.69, −0.54)
J11045701−7715569	T16			M3	II	Hot	M3	M16b	−0.53 (−0.59, −0.47)
J11062554−7633418	ESOHα559			M5.25	II	Cool	M5.5	M16b	−0.91 (−1.01, −0.81)
J11062942−7724586				M6	II	Cool	M6	L07	−1.12 (−1.66, −1.00)
J11063276−7625210	CHSM7869			M6	II	Cool	M6.5	M16b	−1.13 (−1.25, −0.97)
J11063945−7736052	ISO79			M5.25	II	Cool	M5	M16b	−0.78[a]
J11064180−7635489	Hn5			M4.5	II	Cool	M5	M16a	−0.78 (−0.86, −0.68)
J11064510−7727023	CHXR20	28.46	KH07	K6	II	Hot	K6	M16b	−0.03 (−0.10, 0.22)
J11065906−7718535	T23			M4.25	II	Cool	M4.5	M16a	−0.71[a]
J11065939−7530559				M5.25	II	Cool	M5.5	M16b	−0.97 (−1.07, −0.87)
J11070925−7718471				M3	II	Hot	M3	L07	−0.52 (−0.58, −0.45)
J11071181−7625501	CHSM9484			M5.25	II	Cool	M5.5	M16b	−0.97 (−1.07, −0.87)
J11071206−7632232	T24			M0.5	II	Hot	M0	M16a	−0.23 (−0.34, −0.12)
J11071330−7743498	CHXR22E			M3.5	II/T	Hot	M4	M14	−0.63 (−0.71, −0.55)
J11071860−7732516	ChaHα9			M5.5	II	Cool	M5.5	M16a	−0.92 (−1.02, −0.82)
J11072074−7738073	T26	4.570	D13	G2	II	Hot	K0	M16b	0.29 (0.23, 0.56)
J11072825−7652118	T27	0.780	D13	M3	II	Hot	M3	M16b	−0.53 (−0.59, −0.47)
J11074245−7733593	ChaHα2	0.167	La08	M5.25	II	Cool	M5.5	M16b	−0.88 (−0.98, −0.77)
J11074366−7739411	T28	28.87	KH07	M0	II	Hot	M1	M16b	−0.31 (−0.43, −0.19)
J11074656−7615174	CHSM10862			M5.75	II	Cool	M6.5	M16b	−1.15 (−1.25, −1.05)
J11075730−7717262	CHXR30B			M1.25	II	Hot	M1.25	L07	−0.31 (−0.43, −0.18)
J11075792−7738449	Sz22	0.500, 17.6	G97, S13	K6	FS	Hot	K5	M16a	−0.01 (−0.06, 0.23)
J11075809−7742413[b]	T30			M2.5	II	Hot	M3	M16b	−0.51 (−0.58, −0.44)
J11080002−7717304	CHXR30A	0.460	La08	K8	II	Hot	K7	M16b	−0.18 (−0.28, −0.07)
J11080148−7742288	VWCha,T31	0.660	D13	K8	II	Hot	K7	M16a	−0.20 (−0.30, −0.11)
J11080297−7738425	ESOHα562	0.280	D13	M1.25	FS	Hot	M1	M16a	−0.20 (−0.29, 0.04)
J11081509−7733531	T33A	2.400	D13	G7	FS	Hot	K0	M16a	0.12 (0.08, 0.16)
J11081850−7730408[b]	ISO138			M6.5	II	Cool	M6.5	M16b	−1.14 (−1.24, −1.03)
J11082238−7730277	ISO143	18.16	KH07	M5	II	Cool	M5.5	M16a	−0.90 (−0.99, −0.79)
J11082570−7716396				M8	II	Cool	M8	L07	−1.51[a]
J11082650−7715550	ISO147			M5.75	II	Cool	M5.5	M16b	−0.96 (−1.06, −0.86)
J11083905−7716042	Sz27			K8	II/T	Hot	K7	M14	−0.08 (−0.15, 0.16)
J11083952−7734166	ChaHα6			M5.75	II	Cool	M6.5	M16a	−0.99 (−1.06, −0.92)
J11085090−7625135	T37			M5.25	II	Cool	M5.5	M16b	−0.90 (−0.99, −0.79)
J11085367−7521359				M1.5	II	Hot	M1	M16b	−0.28 (−0.39, −0.16)
J11085464−7702129	T38			M0.5	II	Hot	M0.5	M16a	−0.18 (−0.26, 0.06)
J11085497−7632410	ISO165			M5.5	II	Cool	M5.5	M16b	−0.91 (−1.00, −0.81)
J11091812−7630292	CHXR79	0.880	D13	M1.25	II	Hot	M0	M16b	−0.18 (−0.28, −0.07)
J11092266−7634320	C1-6			M1.25	II	Hot	M1	M16b	−0.25 (−0.33, −0.01)
J11092379−7623207	T40			K6	II	Hot	M0.5	M16a	−0.29 (−0.40, −0.18)
J11094260−7725578	C7-1			M5	II	Cool	M5	L07	−0.77[a]
J11094621−7634463	Hn10e	19.17	KH07	M3.25	II	Hot	M3	M16b	−0.47 (−0.54, −0.39)
J11094742−7726290	B43,ISO207			M3.25	II	Hot	M1	M16b	−0.22 (−0.30, 0.02)
J11095215−7639128	ISO217			M6.25	II	Cool	M6.25	L07	−1.20 (−1.76, −1.08)
J11095336−7728365	ISO220			M5.75	II	Cool	M5.5	M16b	−0.96 (−1.06, −0.86)
J11095340−7634255	T42			K5	II	Hot	K7	M16b	−0.12 (−0.21, −0.03)
J11095407−7629253	T43	0.780	D13	M2	II	Hot	M1	M16b	−0.21 (−0.30, 0.03)

Table 1
(Continued)

2MASS	Other Name	Multiplicity (arcsec)	Ref.	Spectral Type Luhman	SED	ALMA Sample	Spectral Type Adopted	Ref.	$\log(M_*)$ $(M_\odot)$
J11095873−7737088	WXCha	0.740	D13	M1.25	II	Hot	M0.5	M16b	−0.29 (−0.39, −0.19)
J11100010−7634578	WWCha	0.006	A15	K5	II	Hot	K0	M16a	0.21 (0.17, 0.27)
J11100369−7633291	Hn11			K8	II	Hot	M0	M16b	−0.14 (−0.23, 0.12)
J11100469−7635452	FNCha			M1	II	Hot	K7	M16a	−0.08 (−0.15, 0.16)
J11100704−7629376	T46	0.120	N12	M0	II	Hot	K7	M16b	−0.14 (−0.24, −0.05)
J11100785−7727480	ISO235			M5.5	II	Cool	M5.5	M16b	−0.89 (−0.99, −0.79)
J11101141−7635292	ISO237	28.32	KH07	K5.5	II	Hot	K5	M16a	0.00 (−0.06, 0.26)
J11103801−7732399	CHXR47	0.170	D13	K3	II	Hot	K4	M16b	0.05 (−0.04, 0.14)
J11104141−7720480	ISO252			M6	II	Cool	M5.5	M16b	−0.96 (−1.06, −0.86)
J11104959−7717517	T47	12.09	KH07	M2	II	Hot	M2	M16b	−0.38 (−0.51, −0.25)
J11105333−7634319	T48			M3.75	II	Hot	M3	M16b	−0.51 (−0.58, −0.44)
J11105359−7725004	ISO256			M4.5	II	Cool	M5	M16b	−0.81 (−0.90, −0.72)
J11105597−7645325	Hn13	0.130	La08	M5.75	II	Cool	M6.5	M16b	−0.98[a]
J11111083−7641574	ESOHα569			M2.5	II	Hot	M1	M16b	−0.31[a]
J11113965−7620152	T49	24.38	KH07	M2	II	Hot	M3.5	M16a	−0.59 (−0.65, −0.53)
J11114632−7620092	CHXN18N			K6	II	Hot	K2	M16a	0.09 (0.05, 0.13)
J11120351−7726009	ISO282			M4.75	II	Cool	M5.5	M16b	−0.89 (−0.98, −0.81)
J11120984−7634366	T50			M5	II	Cool	M5	M16b	−0.78 (−0.84, −0.72)
J11122441−7637064	T51	1.970	D13	K3.5	II	Hot	K2	M16a	0.04 (0.00, 0.10)
J11122772−7644223	T52	11.18	KH07	G9	II	Hot	K0	M16a	0.20 (0.15, 0.25)
J11123092−7644241[b]	T53			M1	II	Hot	M0.5	M16b	−0.17 (−0.26, 0.09)
J11124268−7722230	T54A	0.240	D13	G8	II/T	Hot	K0	M16a	0.20 (0.16, 0.25)
J11124861−7647066	Hn17			M4	II	Cool	M4.5	M16a	−0.69 (−0.77, −0.60)
J11132446−7629227[b]	Hn18			M3.5	II	Hot	M4	M16a	−0.62 (−0.69, −0.54)
J11142454−7733062	Hn21W	5.480	D13	M4	II	Cool	M4.5	M16a	−0.71 (−0.79, −0.63)
J11160287−7624533	ESOHα574			K8	II	Hot	K8	L07	−0.19[a]
J11173700−7704381	Sz45			M0.5	II/T	Hot	M0.5	M14	−0.28 (−0.39, −0.17)
J11175211−7629392				M4.5	II	Cool	M4.5	L07	−0.69 (−0.77, −0.61)
J11183572−7935548				M4.75	II/T	Cool	M5	M16b	−0.77[a]
J11241186−7630425				M5	II/T	Cool	M5.5	M16b	−0.90 (−0.99, −0.79)
J11432669−7804454				M5	II	Cool	M5.5	M16b	−0.86 (−0.93, −0.79)

References. (A15) Anthonioz et al. (2015); (D13) Daemgen et al. (2013); (G97) Ghez et al. (1997); (KH07) Kraus & Hillenbrand (2007); (La08) Lafreniere et al. (2008); (L07) Luhman (2007); (M14) Manara et al. (2014); (M16a), Manara et al. (2016a); (M16b) C. Manara et al. (2016, in preparation); (N12) Nguyen et al. (2012); (S13) Schmidt et al. (2013).

Notes.

[a] For these stars we fixed the isochrone; hence, there are no uncertainties associated with the estimated stellar mass. See Section 2.1.

[b] T30 is the secondary of T31 at a separation of 16″52. *ISO* 138 is the secondary of *ISO* 143 at 18″16. T53 is the secondary of T52 at 11″18. Hn18 is the secondary of CHXR60 (not included in our ALMA survey) at a separation of 28″28.

(This table is available in machine-readable form.)

properties inferred from the VLT spectra are summarized in Manara et al. (2014, 2016a) and C. Manara et al. (2016, in preparation). For eight sources, typically late M dwarfs, these new spectra either were not acquired or lacked enough signal-to-noise ratio (S/N) to reliably derive stellar and accretion properties; hence, we adopt here the spectral type classification and stellar properties reported in Luhman (2007, 2008) (see Table 1). As discussed in Manara et al. (2016a) and C. Manara et al. (2016, in preparation), the difference between the new and literature spectral type is in most cases less than a spectral subclass. The largest difference occurs for the K-type stars and is thought to arise from the lack of good temperature diagnostics in the low-resolution red spectra used in previous studies for spectral classification.

2.1. Stellar Mass Estimates

To derive stellar masses (and ages), we followed the standard approach of comparing empirical effective

temperatures and stellar luminosities to those predicted by pre-main-sequence evolutionary models. Effective temperatures and luminosities for our ALMA Chamaeleon I sample are taken from Manara et al. (2014, 2016a), C. Manara et al. (2016, in preparation), and Luhman (2007, 2008), as summarized in column 9 of Table 1. The H-R diagram is shown in Figure 1, with each object represented by an open circle and the evolutionary tracks from Baraffe et al. (2015) and the nonmagnetic tracks from Feiden (2016) in solid (isochrones) and dashed (stellar mass tracks) lines.

Our choice of evolutionary tracks is motivated by the recent work of Herczeg & Hillenbrand (2015), who demonstrated that these new models better match empirical stellar loci for low-mass stars and brown dwarfs in nearby young associations than older models. In addition, they yield very similar ages for low-mass stars (see Figure 4 in Herczeg & Hillenbrand 2015); hence, they can be combined to extend the stellar mass coverage. This is critical for our Chamaeleon I sample, which,
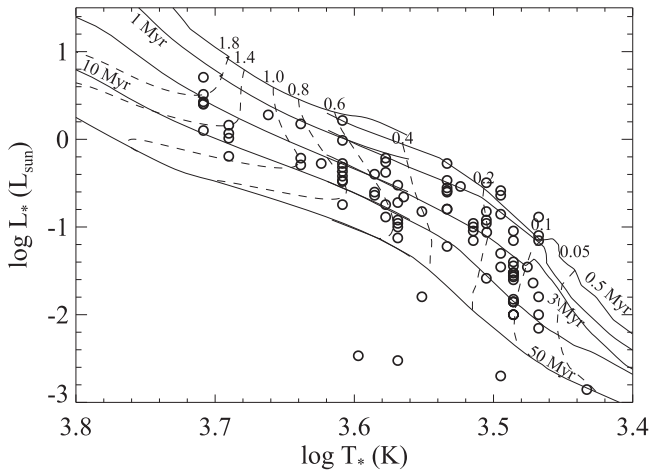
Figure 1. H-R diagram of our ALMA Chamaeleon I sample (each source is represented by an open circle). The nonmagnetic evolutionary tracks from Feiden (2016) are plotted for effective temperatures greater than 3700 K (spectral type M1 and earlier) and masses greater than 0.5 $M_\odot$. For effective temperatures lower than 4200 K and masses lower than 0.5 $M_\odot$ we plot the evolutionary tracks from Baraffe et al. (2015). Note the similarity of the two sets of isochrones in the overlapping effective temperature region for ages ⩾1 Myr.

as shown in Figure 1, spans a large range in stellar mass, from above 1.5 $M_\odot$ down to the substellar regime.[16]

Following Andrews et al. (2013), we adopt a Bayesian inference approach to assign a stellar mass, an age, and associated uncertainties to each of our ALMA targets. The first step in this approach is to interpolate the Baraffe et al. (2015) and Feiden (2016) models on a common, finely sampled age grid. Based on the Chamaeleon I H-R diagram in Figure 1, we include the earliest isochrones at 0.5 Myr through to 50 Myr old isochrones with a step of 0.01 in log scale. Stellar masses are also sampled with the same spacing in log scale. We use the Baraffe et al. (2015) tracks for all objects with effective temperatures ⩽3900 K (M dwarfs) and switch to the Feiden (2016) tracks for hotter stars (spectral types K and earlier). This procedure is motivated by the fact that around ∼3900 K the two sets of isochrones nicely overlap even for 1 Myr old stars (see Figure 4 in Herczeg & Hillenbrand 2015), although there remains a small mismatch at the earliest 0.5 Myr isochrone (see Figure 1).

For each ALMA target, identified by a temperature T_* and luminosity L_* in the H-R diagram, we compute a conditional likelihood function, assuming uniform priors on the model parameters, as

$$F(\hat{T}, \hat{L}|T_*, L_*) = \frac{1}{2\pi\sigma_{T_*}\sigma_{L_*}} \exp\left(-0.5\right.$$
$$\left.\times \left[\frac{(T_* - \hat{T})^2}{\sigma_{T_*}^2} + \frac{(L_* - \hat{L})^2}{\sigma_{L_*}^2}\right]\right), \quad (1)$$

where $\hat{T}$ and $\hat{L}$ are the model grid temperatures and luminosities, while σ_{T_*} and σ_{L_*} are the uncertainties associated with T_* and L_*. The uncertainty in $\log(T_*)$ is assumed to be 0.02 for spectral type earlier than M3 and 0.01 for later spectral type, while the uncertainty in $\log(L_*)$ is taken to be 0.1 (see C.
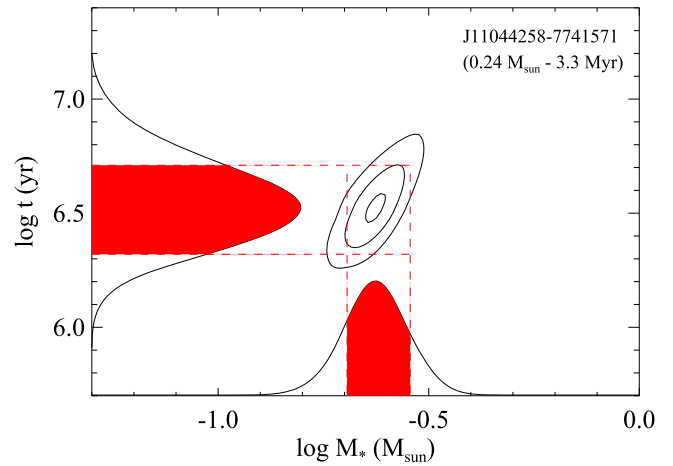

Figure 2. Example of the likelihood function used to estimate stellar masses and ages. The best-fit parameters for J11044258–7741571 are listed on the top right of the panel. The 68% confidence intervals are the red regions of the marginal probability density functions. These regions are calculated from the cumulative integral such that the area above and below the best-fit parameter are each 0.34.

Manara et al. 2016, in preparation). We then integrate $F(\hat{T}, \hat{L}|T_*, L_*)$ over the age and mass covered by the model grids and obtain two marginal probability density functions; see the curves in Figure 2. The best-fit mass and age are the peaks of these functions, and the uncertainties are the values that encompass 68% of the area under the functions.

This approach could be applied to all but nine sources for which age estimates are found to be at the boundary of our grid. For the four sources for which our method identifies the youngest 0.5 Myr isochrone and that appear overluminous in the H-R diagram,[17] we choose this isochrone and compute the stellar mass based solely on the stellar effective temperature. For the other five sources[18] for which our method gives the oldest isochrone of 50 Myr we take the median age of our Chamaeleon I sources and again compute stellar masses based solely on stellar effective temperatures. Three out of these five "old" sources (J10533978–7712338, J11111083–7641574, and J11160287–7624533) have SED and/or spatially resolved imagery suggesting that the central star is surrounded by an edge-on disk (Luhman 2007; Robberto et al. 2012), thus explaining why they appear underluminous in the H-R diagram. We note that our ALMA sample has a median age of 3.5 Myr, slightly older than the previously computed median age (Luhman 2007). The resulting masses and their uncertainties, when available, are reported in the last column of Table 1.

3. OBSERVATIONS AND DATA REDUCTION

Our observations were carried out as part of the ALMA Cycle 2 campaign on 2014 May 1–3 UTC (54 sources) and on 2015 May 18–19 UTC (39 sources). The 2014 observations included all stars with spectral type from Luhman equal to or earlier than M3 (hereafter *Hot* sample), while in 2015 we observed the remaining later spectral type sources (hereafter *Cool* sample).

---

[16] The Feiden (2016) tracks cover from 0.09 to 5.7 $M_\odot$, while the Baraffe et al. (2015) tracks cover from 0.015 to 1.4 $M_\odot$; hence, they are the only ones available in the substellar regime.

[17] J11065906–7718535, J11094260–7725578, J11105597–7645325, and J11183572–7935548.
[18] J10533978–7712338, J11063945–7736052, J11082570–7716396, J11111083–7641574, and J11160287–7624533.

<div align="center">

Table 2
ALMA Observations

</div>

UTC Date	Number of Antennas	Baseline Range (m)	pwv (mm)	Calibrators		
				Flux	Passband	Phase
2014 May 1–3	37	17–558	0.6	Pallas	J1427–4206	J1058–8003
2015 May 18–19	39	21–556	0.6	Ganymede, J1107–448	J0538–4405, J1337–1257	J1058–8003

All observations were obtained in Band 7 with a spatial resolution of $0\rlap{.}{''}7 \times 0\rlap{.}{''}5$; see Table 2 for details on the number of 12 m antennas, baselines, and calibrators. Each science block (SB), comprising either all *Hot* or *Cool* sources plus any calibrator, was executed twice. The correlator was configured to record dual polarization with three continuum basebands of 5.6 GHz aggregated bandwidth centered at 330.0, 341.1, and 343.0 GHz for an average frequency of 338 GHz (887 μm). The fourth baseband was devoted to the serendipitous detection of gas lines and was split into two sub-bands of 0.1 GHz each centered at 329.3 and 330.6 GHz to cover the $C^{18}O$ (3–2) and the ^{13}CO (3–2) transitions. This paper focuses on the continuum data; the reduction and analysis of the CO data will be presented in a separate contribution (F. Long et al. 2016, in preparation). Exposure times for the *Hot* sample were set to achieve a 1σ rms of 1 mJy beam^{-1} in the aggregated continuum bandwidth, while for the *Cool* sample we required 0.2 mJy beam^{-1}. As a comparison previous single-dish millimeter observations of the Chamaeleon I star-forming region had 1σ sensitivities greater than 10 mJy over a beam of $\sim 20''$ (Henning et al. 1993; Belloche et al. 2011).

The ALMA data were calibrated using the CASA software package. The initial reduction scripts were provided by the North American ALMA Science Center and included phase, bandpass, and flux calibration. We reran the scripts using CASA 4.3.1. We used Pallas as the flux calibrator for the *Hot* sample SBs, Ganymede for the first *Cool* sample SB, and the quasar J1107–448 for the second *Cool* sample SB. The flux scale was within 5% and 8% of the two SBs for the *Hot* and *Cool* samples, respectively. For both samples, we used the average of the two SB fluxes in the calibration script. In the analysis that follows we adopt a conservative 1σ uncertainty of 10% on the absolute flux scale.

Dirty continuum images were created from the calibrated visibilities using CASA v4.4 and natural weighting and by averaging the three continuum basebands (see Figures 3(b)–(f) in the electronic version of the paper). We computed the rms of each image in a region outside the expected target location and found a median of 0.99 and 0.23 mJy beam^{-1} for the *Hot* and *Cool* samples, respectively, very close to the requested sensitivities. We also computed an initial flux density at the target location by integrating within the 3 rms closed contour. This flux density, in combination with the image rms and visual inspection, was used to decide whether a source is detected. With this approach we classified 45/54 *Hot* and 21/39 *Cool* targets as detected.

We also identified 10 bright *Hot* and two bright *Cool* sources with S/N ranging from 36 to 100 and rms larger than 2 times the median rms that would benefit from self-calibration. For these 12 sources[19] we followed the steps

suggested by the North American ALMA Science Center for the brightest of our targets, J11100010–7634578. From each of the 12 measurement sets we produced an image with Briggs robust weighting parameter of zero and cell size $0\rlap{.}{''}075$. First, we performed a shallow cleaning on each image, down to a threshold of about 5 times the median rms of the *Hot* or *Cold* sample, and saved the model in the measurement set header. We then calibrated the phases using the model data column, applied the new calibration to the measurement set, and produced a new image from the better-calibrated data. We repeated the cycle of cleaning and phase calibration a second time starting from the new image and by applying a deeper cleaning, down to about 3 times the median rms of the *Hot* or *Cold* sample. The image produced in this second cycle was cleaned a third time, with phases and amplitudes calibrated and applied to the original measurement set. With this approach we found that the final image rms always improved, reaching the median value of ~ 1 mJy beam^{-1} for the *Hot* and ~ 0.2 mJy beam^{-1} for the *Cold* samples even for the brightest of our sources, J11100010–7634578, whose initial image rms was ~ 24 mJy beam^{-1}. The 12 phase- and amplitude-calibrated measurement sets are used in the following steps to compute the source parameters.

4. RESULTS

To compute the flux densities and to determine whether the emission is spatially resolved, we rely on the visibility data as, e.g., discussed in Carpenter et al. (2014). First, we fit all of our 66 detections with an elliptical Gaussian using the *uvmodelfit* task in CASA. This model has six free parameters: the integrated flux density, the offsets in right ascension and declination from the phase center, the FWHM, the aspect ratio, and the position angle. With the underlying assumption that the model describes well the data, we scale the uncertainties on the fitted parameters by the factor needed to produce a reduced χ^2 of 1. If the ratio of the FWHM to its uncertainty is less than 2, which happens for 32 sources, we also fit the visibility data with a point-source model that has only three free parameters: the integrated flux density and the offsets in right ascension and declination from the phase center. For 25 out of 32 sources we find that the reduced χ^2 of the point-source model is less than that of the Gaussian model; hence, we adopt the point-source fits. Even for the seven sources where the reduced χ^2 of the Gaussian model is lower than that of a point-source model, we adopt the point-source fits because the difference in the models' reduced χ^2 is much smaller than the uncertainty on their values, which is approximately $\sqrt{2/N}$ for the over 7000 visibility points that are fitted. Finally, for the 27 sources that are not detected we also fit a point-source model keeping the offsets in right ascension and declination fixed to $-0\rlap{.}{''}3$ and

---

[19] The 10 *Hot* sources that require self-calibration are J10581677–7717170, J10590699–7701404, J11022491–7733357, J11040909–7627193, J11074366–7739411, J11080297–7738425, J11081509–7733531, J11092379–7623207, J11094742–7726290, and J11100010–7634578, while the two *Cold* sources are J11004022–7619280 and J11062554–7633418.
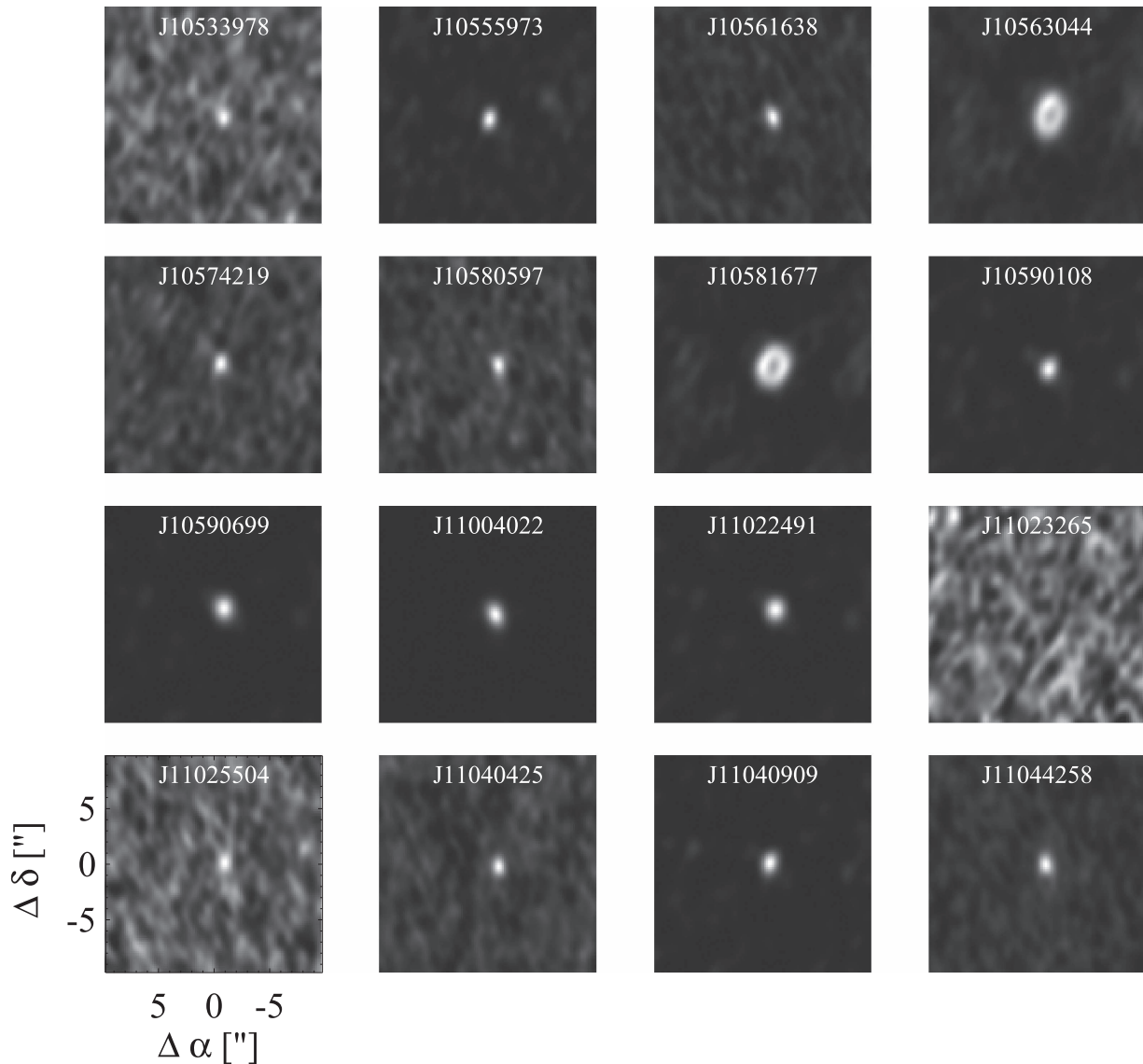
Figure 3. ALMA 887 μm continuum dirty images for our Chamaeleon I sources. The pixel scale is $0\rlap{.}''075$. Note that source flux densities and upper limits were computed from a fit to the visibility data and not from these images; see Section 4 for details.

(An extended version of this figure is available.)

$0\rlap{.}''0$, respectively, the median values from the sources that are detected.

To visualize the goodness of the fits, we compare the best-fit model (solid line) to the real component of the observed visibilities (filled circles) as a function of projected baseline length (UV distance); see Figure 4 as an example (Figures 4 (b)–(f) are available only in the electronic version). In these figures all visibilities are recentered to the continuum centroids found with *uvmodelfit*, each visibility point is the average of the visibilities within a $30\,\mathrm{k}\lambda$ range, and the error bars are the standard deviation divided by $\sqrt{N-1}$, where N is the number of visibility points in the same range. About half of the detected sources have spatially resolved emission, as evidenced by visibilities that decline in amplitude with increasing UV distance. Among them, J10563044–7711393 and J10581677–7717170 have resolved dust cavities; hence, the Gaussian fit discussed above does not provide a good estimate for the source flux density. For these two sources we compute flux densities within the 3σ contour in the deconvolved image;[20] see Figure 5. J10581677–7717170 is a known transition disk with an estimated dust cavity of $\sim$30 au in radius (Kim et al. 2009). On the contrary, J10563044–7711393 has not been classified as a transition disk based on its infrared photometry, but a *Spitzer*/IRS spectrum could not be extracted for this source due to its faintness (Manoj et al. 2011). The radius of both cavities is $\sim$45 au as measured from the images and from the location of the first null in the visibility plot (see Equation (A9) in Hughes et al. 2007).

Overall, we have identified two sources with dust disk cavities, 32 sources whose millimeter emission is resolved (elliptical Gaussian model), 32 sources with unresolved millimeter emission (point source model), and 27 sources with too faint or absent millimeter emission to be detected in our

---

[20] We remind the reader that J10581677–7717170 was one of the sources that required self-calibration (see Section 3); hence, the flux density is computed on the final phase- and amplitude-calibrated image.
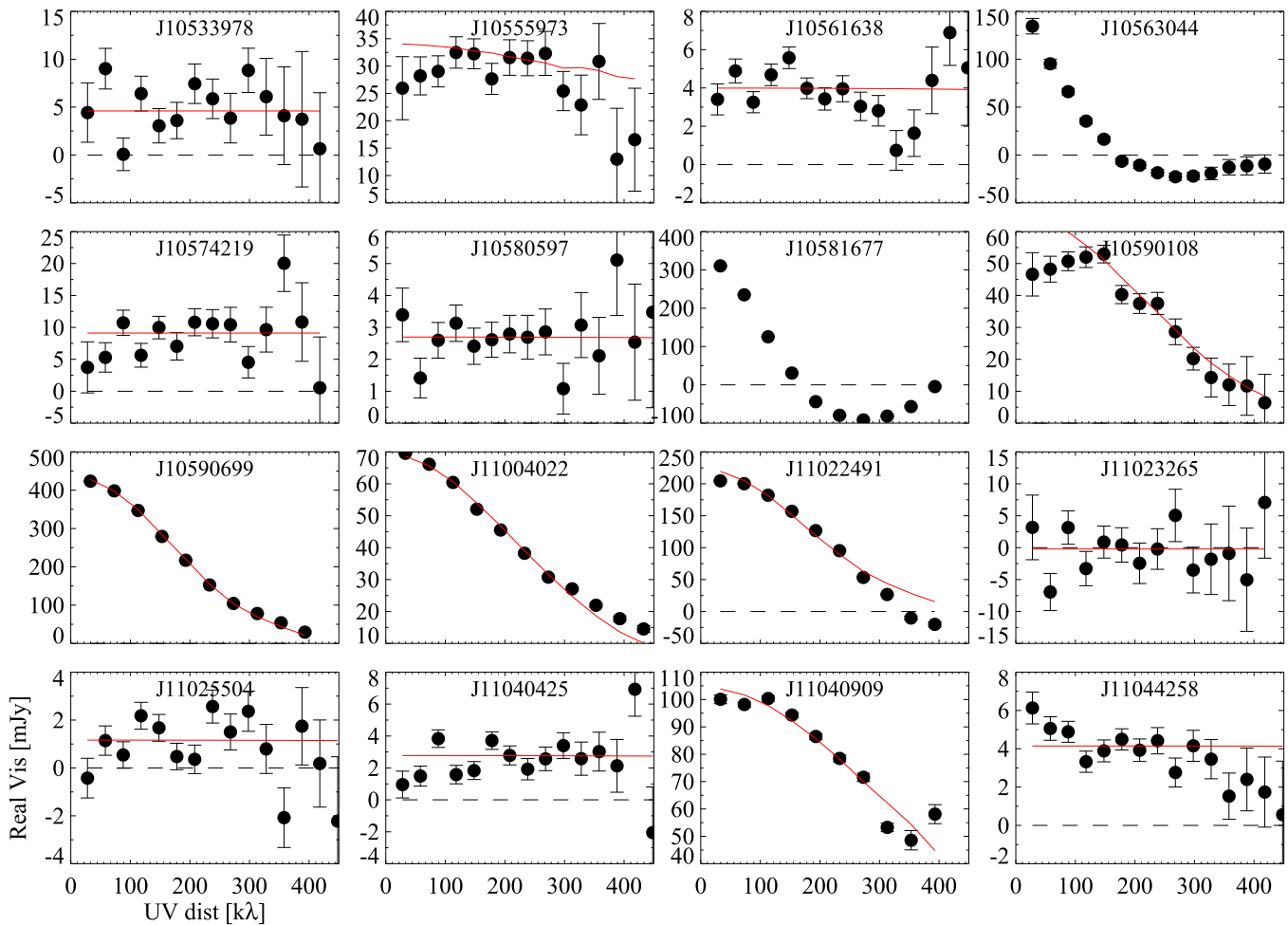
Figure 4. Real part of the observed visibility (circles) as a function of the projected baseline using a sampling of 30 kλ. The best model fit to the data (red solid line) is shown for all targets except the two disks with resolved cavities; see text for details. Similar figures for all other targets are available online.

(An extended version of this figure is available.)

survey. Among the resolved millimeter sources, 23 belong to the *Hot* sample and 9 to the *Cool* sample, implying that ~51% and 39% of the detected sources are resolved in the two samples, respectively. Table 3 summarizes the measured continuum flux densities (F_ν) and uncertainties, offsets from the phase center in right ascension and declination for the detected sources ($\Delta\alpha$ and $\Delta\delta$), and FWHMs for the resolved millimeter sources. In the analysis that follows we calculate upper limits for sources that are not detected as 3 times the uncertainty on F_ν, which is also reported in Table 3.

Flux densities and upper limits as a function of stellar masses are shown in Figure 6 in a log–log plot, with circles for detections and downward-pointing triangles for nondetections. Note that the SED-identified transition disks are not among the brightest millimeter disks. Two of them, J11071330–7743498 (spectral type M3.5) and J11124268–7722230 (spectral type G8), remain undetected at our sensitivity. However, the latter source has also a ~0.7 $M_\odot$ companion at a projected distance of 38 au (Daemgen et al. 2013) that might have tidally truncated the disk of the primary, leading to a lower than average millimeter flux. The disks around J11100704–7629376 and J11103801–7732399, two K-type stars with companions at ~20 and 27 au distance, respectively, also appear fainter than disks around stars of similar stellar mass and might have been truncated. Stars in Taurus with companions at tens of au have

also fainter disks than expected for their mass (Harris et al. 2012). At the other extreme, the star J11100010–7634578 has a companion at 65 mas and the brightest millimeter disk, in this case a circumbinary disk. Circumbinary disks are also found to be among the brightest millimeter disks in Taurus (Harris et al. 2012).

Figure 6 demonstrates that millimeter fluxes have a spread of more than 1 dex at a given stellar mass, part of which, as mentioned above, may be attributed to stellar multiplicity. In spite of the spread, flux densities are strongly correlated with stellar mass. This trend is not unique to the Chamaeleon I star-forming region (Andrews et al. 2013; Mohanty et al. 2013; Ansdell et al. 2016; Barenfeld et al. 2016). Assuming a linear relationship in the log–log plane, we can determine the best fit using the Bayesian method developed by Kelly (2007) that properly accounts for the measurement uncertainties, nondetections, and intrinsic scatter. This Bayesian method assumes Gaussian measurement errors; hence, we have adopted the full range of the stellar mass uncertainty, covering 68% of the area under the marginal probability density function, and divided it by 2 as the error on each stellar mass. For the 10 sources where we had to fix the isochrone we use the median uncertainty in $\log(M_*)$ of ±0.1 dex. With this approach we find the following best-fit relationship: $\log(F_{\mathrm{mm}}/\mathrm{mJy}) = 1.9(\pm0.2) \times \log(M_*/M_\odot) + 1.6(\pm0.1)$.

Table 3
Measured Continuum Flux Densities

2MASS	F_ν (mJy)	$\Delta\alpha$ (arcsec)	$\Delta\delta$ (arcsec)	FWHM (arcsec)
J10533978–7712338	4.60 ± 0.79	−0.37 ± 0.03	−0.09 ± 0.05	...
J10555973–7724399	34.10 ± 1.32	−0.06 ± 0.01	−0.14 ± 0.01	0.18 × 0.11
J10561638–7630530	3.99 ± 0.16	−0.37 ± 0.01	−0.08 ± 0.01	...
J10563044–7711393[a]	117.58 ± 1.10	...	...	...
J10574219–7659356	9.12 ± 0.83	−0.27 ± 0.02	0.04 ± 0.03	...
J10580597–7711501	2.68 ± 0.16	−0.38 ± 0.01	−0.01 ± 0.02	...
J10581677–7717170[a]	310.18 ± 1.00	...	...	...
J10590108–7722407	65.34 ± 1.70	−0.40 ± 0.01	−0.15 ± 0.01	0.40 × 0.33
J10590699–7701404	442.18 ± 0.76	−0.39 ± 0.00	0.21 ± 0.00	0.51 × 0.44
J11004022–7619280	69.75 ± 0.17	−0.28 ± 0.00	−0.01 ± 0.00	0.38 × 0.35
J11022491–7733357	225.68 ± 0.74	−0.44 ± 0.00	0.15 ± 0.00	0.45 × 0.45
J11023265–7729129	−0.21 ± 0.82	...	...	...
J11025504–7721508	1.16 ± 0.16	−0.41 ± 0.03	0.04 ± 0.04	...
J11040425–7639328	2.77 ± 0.16	−0.39 ± 0.01	−0.11 ± 0.02	...
J11040909–7627193	104.78 ± 0.60	−0.25 ± 0.00	0.03 ± 0.00	0.25 × 0.25
J11044258–7741571[b]	4.15 ± 0.16	−0.29 ± 0.01	−0.03 ± 0.01	...
J11045701–7715569	2.54 ± 0.81	−0.32 ± 0.07	−0.01 ± 0.09	...
J11062554–7633418	46.05 ± 0.15	−0.43 ± 0.00	−0.05 ± 0.00	0.23 × 0.15
J11062942–7724586	0.25 ± 0.16	...	...	...
J11063276–7625210	−0.01 ± 0.16	...	...	...
J11063945–7736052	0.37 ± 0.16	...	...	...
J11064180–7635489	0.97 ± 0.16	−0.37 ± 0.03	−0.23 ± 0.05	...
J11064510–7727023	0.53 ± 0.82	...	...	...
J11065906–7718535	24.28 ± 0.35	−0.47 ± 0.00	0.12 ± 0.00	0.17 × 0.15
J11065939–7530559	3.11 ± 0.16	−0.30 ± 0.01	−0.04 ± 0.01	...
J11070925–7718471	0.06 ± 0.82	...	...	...
J11071181–7625501	0.03 ± 0.16	...	...	...
J11071206–7632232	4.23 ± 0.81	−0.42 ± 0.04	−0.03 ± 0.06	...
J11071330–7743498	0.42 ± 0.81	...	...	...
J11071860–7732516	0.93 ± 0.16	−0.46 ± 0.03	0.12 ± 0.05	...
J11072074–7738073	26.36 ± 1.46	−0.31 ± 0.01	0.02 ± 0.01	0.29 × 0.29
J11072825–7652118	1.50 ± 0.81	...	...	...
J11074245–7733593	2.37 ± 0.41	−0.40 ± 0.03	−0.02 ± 0.04	0.34 × 0.30
J11074366–7739411	107.27 ± 0.56	−0.28 ± 0.00	0.02 ± 0.00	0.26 × 0.19
J11074656–7615174	2.18 ± 0.16	−0.31 ± 0.01	0.09 ± 0.02	...
J11075730–7717262	6.47 ± 0.80	−0.34 ± 0.03	0.02 ± 0.04	...
J11075792–7738449	19.85 ± 1.48	−0.18 ± 0.01	0.00 ± 0.02	0.33 × 0.33
J11075809–7742413	6.45 ± 0.79	−0.23 ± 0.03	−0.11 ± 0.04	...
J11080002–7717304	−0.69 ± 0.80	...	...	...
J11080148–7742288	44.37 ± 0.82	−0.20 ± 0.00	0.31 ± 0.01	...
J11080297–7738425	102.24 ± 0.58	−0.30 ± 0.00	−0.07 ± 0.00	0.28 × 0.28
J11081509–7733531	209.29 ± 0.43	1.00 ± 0.00	−0.26 ± 0.00	0.46 × 0.46
J11081850–7730408	0.26 ± 0.16	...	...	...
J11082238–7730277[b]	0.23 ± 0.16	...	...	...
J11082570–7716396	0.23 ± 0.15	...	...	...
J11082650–7715550	−0.24 ± 0.16	...	...	...
J11083905–7716042	14.11 ± 0.79	−0.36 ± 0.01	0.04 ± 0.02	...
J11083952–7734166	0.02 ± 0.16	...	...	...
J11085090–7625135	−0.04 ± 0.16	...	...	...
J11085367–7521359	24.60 ± 1.37	−0.21 ± 0.01	0.01 ± 0.01	0.30 × 0.22
J11085464–7702129	3.90 ± 0.79	−0.38 ± 0.04	−0.05 ± 0.06	...
J11085497–7632410	0.46 ± 0.16	...	...	...
J11091812–7630292	1.30 ± 0.79	...	...	...
J11092266–7634320	3.85 ± 0.78	−0.24 ± 0.04	−0.26 ± 0.06	...
J11092379–7623207	123.11 ± 0.57	−0.30 ± 0.00	−0.07 ± 0.00	0.26 × 0.23
J11094260–7725578	0.37 ± 0.16	...	...	...
J11094621–7634463	4.73 ± 0.79	−0.37 ± 0.03	−0.08 ± 0.05	...
J11094742–7726290	147.85 ± 0.86	−0.42 ± 0.00	−0.08 ± 0.00	0.75 × 0.45
J11095215–7639128	0.37 ± 0.16	...	...	...
J11095336–7728365	0.29 ± 0.16	...	...	...
J11095340–7634255	76.10 ± 1.83	−0.34 ± 0.01	0.06 ± 0.01	0.56 × 0.38
J11095407–7629253	30.49 ± 1.24	−0.36 ± 0.01	−0.17 ± 0.01	0.13 × 0.13
J11095873–7737088	20.81 ± 0.57	−0.53 ± 0.01	−0.10 ± 0.01	...

Table 3
(Continued)

2MASS	F_ν (mJy)	$\Delta\alpha$ (arcsec)	$\Delta\delta$ (arcsec)	FWHM (arcsec)
J11100010−7634578	1363.47 ± 0.82	−0.40 ± 0.00	−0.03 ± 0.00	0.56 × 0.44
J11100369−7633291	9.83 ± 0.79	−0.32 ± 0.02	−0.02 ± 0.02	...
J11100469−7635452	7.73 ± 0.78	−0.36 ± 0.02	0.04 ± 0.03	...
J11100704−7629376	7.17 ± 0.78	−0.35 ± 0.02	0.09 ± 0.03	...
J11100785−7727480	0.49 ± 0.16	...	...	...
J11101141−7635292	73.82 ± 1.40	−0.41 ± 0.00	0.07 ± 0.00	0.19 × 0.16
J11103801−7732399	5.37 ± 0.78	−0.26 ± 0.03	0.09 ± 0.04	...
J11104141−7720480	−0.00 ± 0.16	...	...	...
J11104959−7717517	58.37 ± 1.45	−0.41 ± 0.00	0.11 ± 0.01	0.34 × 0.21
J11105333−7634319	31.02 ± 1.29	−0.33 ± 0.01	0.01 ± 0.01	0.22 × 0.18
J11105359−7725004	7.88 ± 0.34	−0.38 ± 0.01	−0.07 ± 0.01	0.18 × 0.13
J11105597−7645325	2.23 ± 0.22	−0.41 ± 0.02	−0.08 ± 0.03	...
J11111083−7641574	54.27 ± 1.75	−0.32 ± 0.01	0.34 ± 0.01	0.74 × 0.16
J11113965−7620152	21.48 ± 0.80	−0.25 ± 0.01	0.38 ± 0.01	...
J11114632−7620092	35.20 ± 1.26	−0.25 ± 0.01	0.43 ± 0.01	0.19 × 0.11
J11120351−7726009	2.95 ± 0.16	−0.42 ± 0.01	0.07 ± 0.02	...
J11120984−7634366	4.44 ± 0.22	−0.37 ± 0.01	0.07 ± 0.01	...
J11122441−7637064	0.19 ± 0.78	...	...	...
J11122772−7644223	59.05 ± 1.29	−0.38 ± 0.00	0.12 ± 0.00	0.12 × 0.10
J11123092−7644241[b]	12.18 ± 0.83	−0.32 ± 0.01	0.25 ± 0.02	...
J11124268−7722230	−0.02 ± 0.79	...	...	...
J11124861−7647066	−0.10 ± 0.16	...	...	...
J11132446−7629227	8.07 ± 0.79	−0.35 ± 0.02	−0.05 ± 0.03	...
J11142454−7733062	7.43 ± 0.34	−0.40 ± 0.01	−0.19 ± 0.01	0.18 × 0.16
J11160287−7624533	12.83 ± 1.68	−0.34 ± 0.03	0.06 ± 0.04	0.43 × 0.43
J11173700−7704381	28.26 ± 1.29	−0.36 ± 0.01	−0.03 ± 0.01	0.20 × 0.20
J11175211−7629392	−0.31 ± 0.16	...	...	...
J11183572−7935548	14.52 ± 0.35	0.18 ± 0.00	−0.32 ± 0.01	0.22 × 0.22
J11241186−7630425	1.47 ± 0.16	−0.35 ± 0.02	−0.12 ± 0.03	...
J11432669−7804454	1.36 ± 0.50	−0.51 ± 0.10	−0.24 ± 0.11	0.53 × 0.50

Notes. Sources with an FWHM reported in the last column of the table are those that were fitted with an elliptical Gaussian. Undetected sources have ellipses in all columns following the flux density column. For these sources flux densities are measured assuming a point-source model and fixed $\Delta\alpha$ and $\Delta\delta$ to the median values of the detected sources.

[a] Sources with rings. Integrated flux density is measured on the image within the 3σ contour.

[b] Sources that have additional millimeter detections in their exposures: J11044258−7741571 (*ISO* 52) at ∼6″, coordinates (11:04:40.59; −77:41:56.9); J11082238−7730277 (*ISO* 143) at ∼10″, coordinates (11:08:21.11; −77:30:18.9); and J11123092−7644241 (T53) at ∼11″, coordinates (11:12:27.7;−76:44:22.3). In the first two cases there is no object in the SIMBAD Astronomical Database associated with the millimeter emission. In the case of T53 we detect the disk from the companion T52. Fluxes from these additional detections are not reported in the table.

(This table is available in machine-readable form.)

Although our 1σ confidence intervals in stellar mass are often not symmetric around the best value, they are still small enough that the assumed Gaussian distribution does not affect the Bayesian fit. We tested that only when the error on $\log(M_*)$ becomes larger than 2.5 times the median value, the best-fit relation is no longer consistent with the one reported here and the inferred slope steepens. This means that the intrinsic scatter in millimeter fluxes drives the best fit given our measurement errors in $\log(F_{\rm mm})$ and $\log(M_*)$. This is also confirmed by other regression methods that do not account for measurement errors but recover the same slope and intercept of the Bayesian approach within the quoted uncertainties (see Appendix). To further test the robustness of this relation, we also compute stellar masses using the effective temperatures and luminosities in Luhman (2007) and find the following best fit: $\log(F_{\rm mm}/{\rm mJy}) = 2.1(\pm0.3) \times \log(M_*/M_\odot) + 1.7(\pm0.2)$, basically consistent with the one using the new stellar properties. Thus, the $F_{\rm mm}$–M_* relation in Chamaeleon I is much steeper than linear, and the millimeter flux scales almost with the square of the stellar mass.

The 1.9–2.1(±0.2) slope of Chamaeleon I is within the 1.5–2.0 range reported for Taurus, where the range in Taurus reflects the use of different evolutionary tracks to assign stellar masses (Andrews et al. 2013). For the old Baraffe et al. (1998) tracks, which in Andrews et al. (2013) are the most similar to the ones we use, the $F_{\rm mm}$–M_* slope in Taurus is 1.5 ± 0.2, lower than but still marginally consistent with the one we find in Chamaeleon I. We caution that lower values can also result from low sensitivity at the lower stellar mass end. As a test we degrade our sensitivity to the typical 850 μm 1σ sensitivity of ∼3 mJy achieved in Taurus, 3 and 15 times worse than the actual sensitivity of the *Hot* and *Cool* samples in Chamaeleon I. The best-fit slope of this degraded data set is only 1.3 ± 0.2, still consistent with the Taurus one but shallower than the slope we measure in Chamaeleon I with the actual sensitivities. This simple test demonstrates the need for deep millimeter surveys to reveal the intrinsic disk flux–stellar mass dependence.
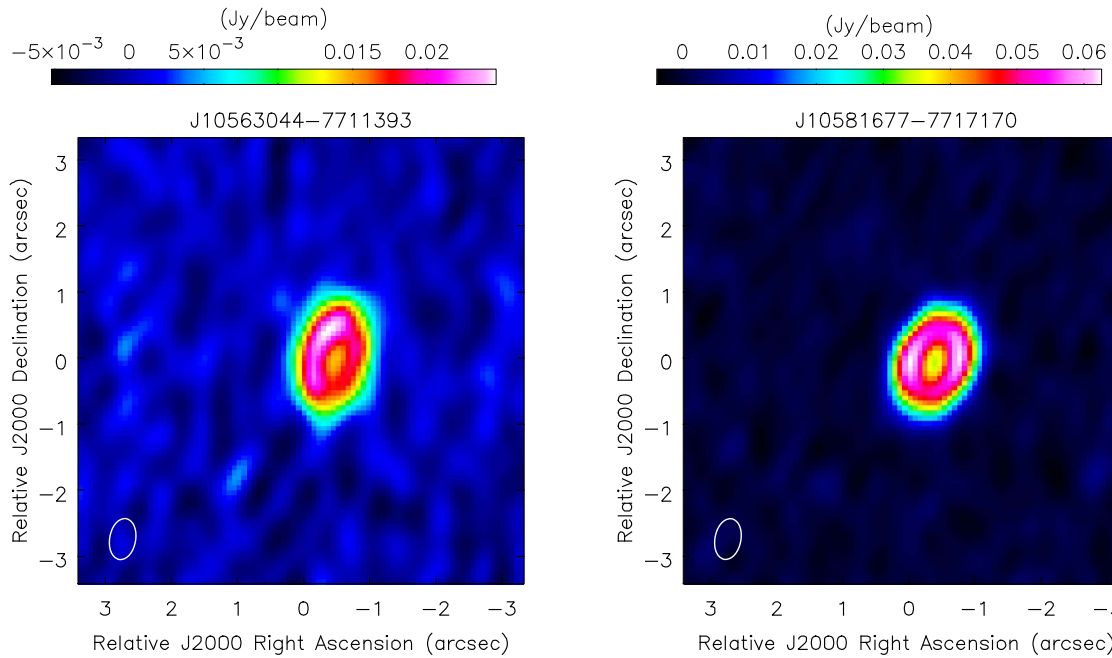
Figure 5. The two disks in our Chamaeleon I sample with spatially resolved dust cavities. J10581677 is a known transition disk based on its infrared photometry and spectroscopy.

5. DUST DISK MASSES

Dust disk emission at millimeter wavelengths is mostly optically thin; hence, continuum flux densities can be used to estimate dust disk masses (e.g., Beckwith et al. 1990). We adopt the simplified approach commonly used in the field (e.g., Natta et al. 2000) and assume isothermal and optically thin emission to compute disk masses as follows:

$$\log M_{\rm dust} = \log F_\nu + 2\log d - \log \kappa_\nu - \log B_\nu(T_{\rm dust}) \quad (2)$$

where F_ν is the flux density at 338 GHz (887 μm), d is the distance (160 pc for Chamaeleon I; Luhman 2008), κ_ν is the dust opacity, and $B_\nu(T_{\rm dust})$ is the Planck function at the temperature $T_{\rm dust}$. We adopt a dust opacity of 2.3 cm^2 g^{-1} at 230 GHz with a frequency dependence of $\nu^{0.4}$, the same as in Andrews et al. (2013) for Taurus and in Carpenter et al. (2014) for Upper Sco. The average dust temperature responsible for the millimeter emission ($T_{\rm dust}$) is poorly constrained. Andrews et al. (2013) performed 2D continuum radiative transfer calculations for a representative grid of disk models and proposed the following scaling relation for stars in the 0.1–100 $L_\odot$ luminosity range: $T_{\rm dust} = 25\,{\rm K} \times (L_*/L_\odot)^{0.25}$. However, van der Plas et al. (2016) and N. Hendler et al. (2016, in preparation) show that a weaker $T_{\rm dust}$–L_* dependence can be reached by adjusting some of the disk input parameters used in Andrews et al. (2013), most notably the outer disk radius. In particular, N. Hendler et al. (2016, in preparation) find that if lower-mass stars have smaller dust disks, then the $T_{\rm dust}$–L_* relation flattens out, becoming almost independent of stellar luminosity if the dust disk radius scales linearly with stellar mass. As discussed in Section 4, the percentage of resolved disks is higher in the *Hot* than in the *Cool* sample, perhaps hinting at smaller dust disks around lower-mass stars. However, this could also be due to low S/N at the low end of the stellar mass spectrum. Because an S/N on the continuum
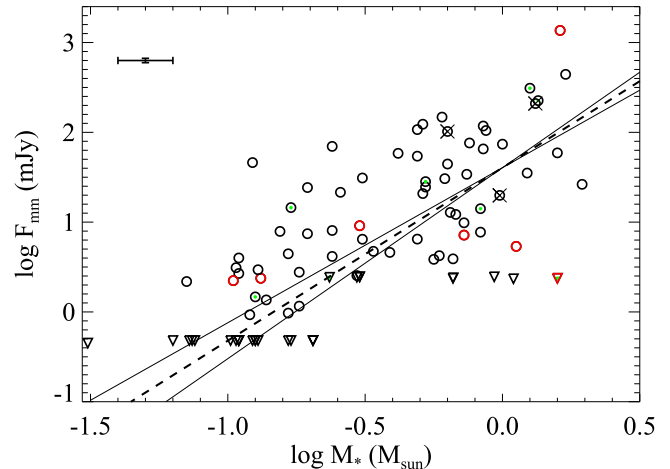
Figure 6. Flux densities ($F_{\rm mm}$) as a function of stellar masses (M_*). Circles are sources with detected millimeter flux, while downward-pointing triangles represent nondetections. Sources marked with a cross are FS disks, a green dot within the main symbol denotes Class II/T SEDs, while a red color denotes "close" binaries (projected separation ⩽40 au). The dashed line gives the best-fit relationship using a Bayesian approach that accounts for censored data. The median error bar in log(M_*) and log($F_{\rm mm}$) is shown in the upper left corner of the plot and corresponds to ±0.1 and ±0.02 dex, respectively.

⩾30 is needed to properly estimate dust disk sizes (Tazzari et al. 2016), deeper ALMA observations are needed to pin down whether and how the disk size scales with stellar mass.

Given the uncertainty in the $T_{\rm dust}$–L_* relation, we compute dust disk masses for two extreme cases: (a) a constant $T_{\rm dust}$ fixed to 20 K to directly compare our results to recent ALMA surveys of other star-forming regions (e.g., Lupus, Ansdell et al. 2016), and (b) a varying $T_{\rm dust}$ with stellar luminosity as proposed by Andrews et al. (2013). Several studies have applied a plateau of ∼10 K to the outer disk temperature (Mohanty et al. 2013; Ricci et al. 2014; Testi et al. 2016), given that this is the value reached by dust grains heated by the

Table 4
$M_{dust}-M_*$ Relations

Region	Age (Myr)	$\alpha_{T_{20}}$	$\beta_{T_{20}}$	α	β	Dispersion
Taurus	1–2	1.6(0.2)	1.2(0.1)	1.1(0.2)	1.0(0.1)	0.7(0.1)
Lupus[a]	1–3	1.8(0.3)	1.6(0.2)	1.1(0.3)	1.4(0.2)	0.8(0.1)
Cha I	2–3	1.9(0.2)	1.1(0.1)	1.3(0.2)	1.1(0.1)	0.8(0.1)
Upper Sco	10	2.7(0.4)	0.9(0.2)	1.9(0.4)	0.8(0.2)	0.7(0.1)

Notes. The listed α and β values (uncertainties in parentheses) are the slope and intercept of the following linear relation: $\log(M_{dust}/M_\oplus) = \alpha \times \log(M_*/M_\odot) + \beta$. The first two entries are obtained assuming a fixed dust temperature of 20 K, while the other entries assume a dust disk temperature scaling with stellar luminosity (see text for more details).
[a] There are 20 sources in Lupus that do not have stellar masses (J. M. Alcalá et al. 2016, in preparation; Ansdell et al. 2016). While Ansdell et al. (2016) have assigned masses in a Monte Carlo fashion following the distribution of the Lupus I–IV YSOs, we do not include these sources in our fits. The slope and dispersion reported in Ansdell et al. (2016) are the same as those reported here.
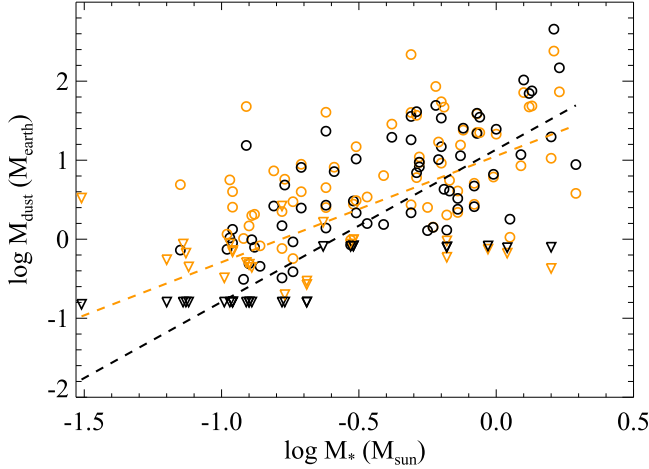
Figure 7. Dust disk masses (M_{dust}) as a function of stellar masses (M_*). Black symbols are for a constant dust disk temperature of 20 K, while orange symbols use the $T_{dust}-L_*$ scaling relation proposed by Andrews et al. (2013). The dashed lines are the best fits for these two cases. Note that the scaling relation proposed by Andrews et al. (2013) flattens the disk–stellar mass relation.

Figure 8. $M_{dust}-M_*$ relation in four different regions: Taurus (green solid line), Lupus (red dot-dashed line), Chamaeleon I (black dashed line), and Upper Sco (light-blue dotted line). These relations are obtained assuming a fixed dust temperature of 20 K (see also Table 4). For Chamaeleon I we also plot the individual dust disk masses. Note that the ~10 Myr old Upper Sco has a steeper $M_{dust}-M_*$ relation than the other star-forming regions.
(The data used to create this figure are available.)

interstellar radiation field in giant molecular clouds (Mathis et al. 1983). We have decided not to apply this plateau in our study for two reasons. First, continuum radiative transfer models show that the interstellar radiation field has a negligible effect on the dust disk temperature and outer disks can be colder than 10 K (N. Hendler et al. 2016, in preparation; van der Plas et al. 2016). Second, Guilloteau et al. (2016) note that the edge-on disk of the Flying Saucer absorbs radiation from CO background clouds and infer very low dust temperatures of 5–7 K at ~100 au in this disk. The lowest-luminosity source in our Chamaeleon I sample, J11082570–7716396 with $L_{bol} = 0.0014\,L_\odot$, has a T_{dust} of 4.8 K with our prescription. Such a value is below 10 K but still consistent with the lower temperatures found in disk models and in the Flying Saucer disk.

Figure 7 summarizes our findings, with black and orange symbols for cases (a) and (b), respectively. A lower T_{dust} for lower-luminosity (typically lower-mass) objects results in a lower Planck function and hence in a higher dust mass estimate. When applying to these two extreme cases the same Bayesian approach described in Section 4, we find the following best fits: $\log(M_{dust}/M_\oplus) = 1.9(\pm0.2) \times \log(M_*/M_\odot) + 1.1(\pm0.1)$ for a constant T_{dust} and $\log(M_{dust}/M_\oplus) = 1.3(\pm0.2) \times \log(M_*/M_\odot) + 1.1(\pm0.1)$ for T_{dust} decreasing with stellar luminosity. The standard deviation (hereafter dispersion)
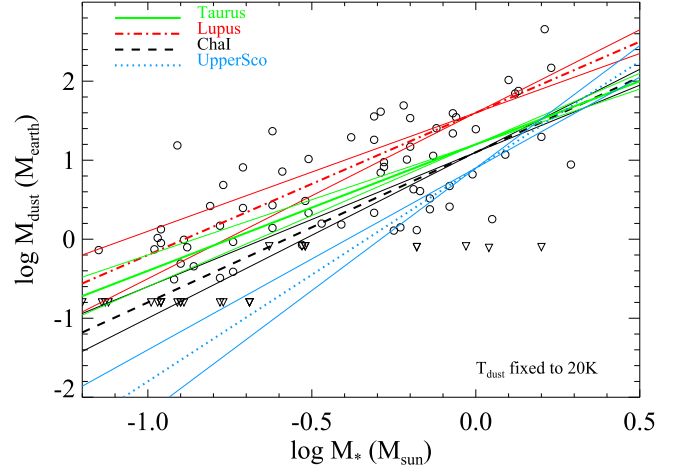
about the regression is 0.8 ± 0.1 dex; see also Table 4. As expected, the slope of the $M_{dust}-M_*$ relation is the same as that of the $F_{mm}-M_*$ relation for the assumption of constant temperature, while it is flatter when the temperature decreases with stellar luminosity. Importantly, even the flatter relation is steeper than the linear one inferred from pre-ALMA disk surveys (Andrews et al. 2013; Mohanty et al. 2013) and from ALMA surveys with a limited coverage of stellar masses (e.g., Carpenter et al. 2014 and Section 4). Most likely the $M_{dust}-M_*$ relation is steeper than $1.3(\pm0.2)$ since our ALMA observations, as well as recent analysis of brown dwarf disks, hint at smaller dust disks around lower-mass stars (N. Hendler et al. 2016, in preparation; Testi et al. 2016). However, quantifying the steepness of the $M_{dust}-M_*$ relation will require measuring how dust disk sizes scale with stellar masses.

6. DISCUSSION

6.1. The Disk–Stellar Mass Scaling Relation in Nearby Regions

The four nearby regions of Taurus ($d = 140\,$pc, age ~ 1–2 Myr; Luhman 2004), Lupus ($d = 140\,$pc, age ~ 1–3 Myr; Comerón 2008), Chamaeleon I ($d = 160\,$pc,

age ~ 2–3 Myr; Luhman 2008), and Upper Sco ($d = 145$, age ~ 5–10 Myr; Slesnick et al. 2008) have ages spanning the range over which significant disk evolution is expected to occur; hence, they have been the focus of many studies to understand when and how protoplanetary material is dispersed. Infrared surveys with the *Spitzer Space Telescope* have established that the fraction of optically thick dust disks, those displaying excess emission at IRAC wavelengths (3.6–4.5 μm), decreases from ~65% in Taurus to ~50% in Lupus and Chamaeleon I and drops to only ~15% in Upper Sco (Ribas et al. 2014). Over the same age range there is tentative evidence for an increase in the frequency of Class II/T SEDs relative to the total disk population, just a few percent at ages $\leqslant$2 Myr and ~10% at older ages (Espaillat et al. 2014). These observations trace the depletion/dispersal of small micron-sized grains within a few au from the star and support a scenario in which protoplanetary material is cleared from inside out (see Alexander et al. 2014 for a recent review on disk dispersal timescales and mechanisms). Millimeter observations probe the population of larger millimeter/centimeter-sized grains at radial distances $\gtrsim$10 au. Thanks to the exquisite sensitivity of ALMA, there are now millimeter surveys that parallel those at infrared wavelengths in sample size, thus enabling testing if significant evolution occurs in the outer disk over the ~1–10 Myr age range.

The disk populations of the Chamaeleon I (this paper), Lupus (Ansdell et al. 2016), and Upper Sco (Barenfeld et al. 2016) regions have been probed with ALMA in Band 7 at similar sensitivity. The Taurus star-forming region has been covered with the SMA at a lower sensitivity (Andrews et al. 2013), about 3 and 15 times lower than that used here for the *Hot* and *Cool* samples, respectively. To compare their $M_{\rm dust}$–M_* relations, we reanalyze all the data sets in a self-consistent manner: we recompute all the stellar masses as discussed in Section 2.1 using the same evolutionary tracks and then apply the approach described in Section 5 to account for millimeter detections and upper limits. The first step is important because, as pointed out in Andrews et al. (2013), different evolutionary tracks can result in slightly different $M_{\rm dust}$–M_* relations. We note that the adopted spectral type–effective temperature scale is essentially the same in all four regions, with a small difference of only ~10 K in the M7–M8 range, where there are only a few, if any, sources in each region. For Upper Sco we only consider disks classified as "Full" and "Transitional" in Table 1 of Barenfeld et al. (2016), equivalent to the Class II and II/T SEDs in Chamaeleon I. More evolved/debris disks, Class III type, are not included in the Taurus, Lupus, and Chamaeleon I millimeter surveys. These disks most likely represent a different evolutionary stage when most of the gas disk has been dispersed (e.g., Pascucci et al. 2006) and the millimeter emission arises from second-generation dust produced in the collision of larger asteroid-size bodies. The resulting $M_{\rm dust}$–M_* relations for these four regions are summarized in Table 4 and plotted in Figure 8 for the case of constant dust temperature. This case is essentially equivalent to comparing submillimeter luminosities as a function of M_* in different star-forming regions (see also Section 5).

Taurus has the shallowest $M_{\rm dust}$–M_* relation among these regions. However, as discussed in Section 4, the lower sensitivity of the survey can account for the apparent difference with Chamaeleon I. Lupus has the same slope but appears to have slightly more massive disks than Taurus and

Chamaeleon I. However, given the few ~1 $M_\odot$ stars in Lupus, the intercept is less well determined than in Taurus and Chamaeleon I. Indeed, adding the 20 obscured Lupus sources by randomly assigning a stellar mass reduces the intercept by 0.3, making the $M_{\rm dust}$–M_* relation of Lupus the same as the one of Taurus (M. Ansdell, private communication) and Chamaeleon I. Hence, we conclude that the same $M_{\rm dust}$–M_* relation is shared by star-forming regions that are 1–3 Myr old. We also note that the relation is steeper than linear. As already pointed out in Barenfeld et al. (2016) and Ansdell et al. (2016), the disk mass distribution in the ~5–10 Myr old Upper Sco association is significantly different from that in Taurus and Lupus, with the mean dust disk mass in the latter two regions being about three times higher than in Upper Sco. By performing a generalized Wilcoxon test[21] with the cendiff command in the NADA R package, we find that the disk mass distribution in Chamaeleon I is indistinguishable from that of Taurus ($p = 52\%$) and Lupus ($p = 8\%$) but different from that of Upper Sco ($p = 0.0001\%$) within the same ~0.1–1.6 $M_\odot$ stellar mass range. The mean dust disk mass is ~10 $M_\oplus$ for Chamaeleon I but only ~4 $M_\oplus$ for Upper Sco under the assumption of constant dust temperature and with our value for the dust opacity. Table 4 shows that the $M_{\rm dust}$–M_* relation is also steeper in Upper Sco than in the other three younger regions (see also Figure 6 in Ansdell et al. 2016). Based on the inferred relations, it appears that disks around 0.5 $M_\odot$ have depleted their dust disk mass in millimeter grains by a factor of 2.5 by ~10 Myr, while disks around 0.1 $M_\odot$ have depleted it by an even larger factor of 5. To further corroborate our finding, we perform the same Wilcoxon test on the disk mass distribution for stars more and less massive than ~0.5 $M_\odot$. The probability that Chamaeleon I and Upper Sco have the same disk mass distribution is as high as 52% for >0.5 $M_\odot$ stars, while it is only 0.02% for the lower stellar mass bin with average masses that are a factor of 2 lower in Upper Sco than in Chamaeleon I. When lowering the stellar mass value to create the two disk mass samples, the probability that the high stellar mass bins in Chamaeleon I and Upper Sco have the same disk mass distribution also decreases, reaching 1% at 0.28 $M_\odot$. This demonstrates that differences in the two distributions are more pronounced toward the lower stellar mass end, well in line with a steeper $M_{\rm dust}$–M_* relation in Upper Sco than in Chamaeleon I.

Finally, it is interesting to note that the dispersion around the $M_{\rm dust}$–M_* relations is very similar in the four regions and amounts to ~0.8 dex. Different disk masses, dust temperatures, and grain sizes can contribute to the dispersion. Whatever the cause, the dispersion does not depend on the environment or age of the region, but seems to be an intrinsic property of the disk population reflecting a range of initial conditions that might, at least in part, account for the diversity of planetary systems.

6.2. On the Evolving Disk–Stellar Mass Scaling Relation

In the previous section we showed that the 1–3 Myr old star-forming regions of Taurus, Lupus, and Chamaeleon I share the same $M_{\rm dust}$–M_* relation, while the older Upper Sco association has a steeper relation. What is the physical process leading to a

---

[21] The null hypothesis is that two groups have the same distribution; p denotes the probability to reject the null hypothesis. Censored data are included in cendiff.
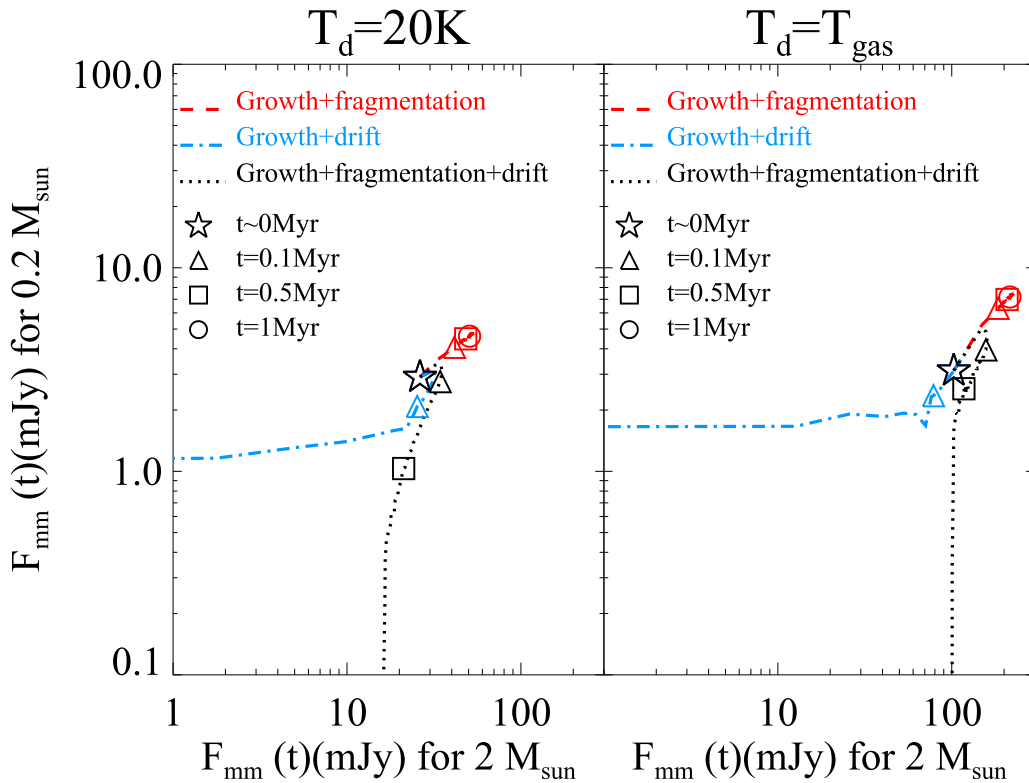
Figure 9. Evolution of the 850 μm flux density for a disk around a 2 $M_\odot$ star (x-axis) and a disk around a 0.2 $M_\odot$ star (y-axis). For both stars, the initial disk mass is set equal to 1% of the stellar mass. The left panel assumes a constant dust temperature through the disk, while the right panel assumes a radially decreasing dust temperature set equal to the gas temperature; see text for details. The growth+fragmentation+drift case can qualitatively explain the observed steepening in the M_{dust}–M_* relation with time.

steepening of the M_{dust}–M_* relation with time? One possibility would be to invoke a stellar-mass-dependent conversion to larger grains, in that disks around lower-mass stars would convert more millimeter grains into larger centimeter grains that go undetected. Alternatively, the higher depletion of millimeter-sized grains toward lower-mass stars could result from more efficient inward drift, i.e., millimeter-sized grains would be still orbiting the star but in the inner and not in the outer disk, where optical depth effects might hide them.

To test these scenarios, we use the Lagrangian code developed by Krijt et al. (2016) and simulate the evolution of dust disk grains subject to (a) growth and fragmentation; (b) growth and radial drift; and (c) growth, radial drift, and fragmentation. In all models, the dust disk initially extends from 2 to 200 au with a power-law surface density with index -1.5, the dust-to-gas mass ratio is 0.01, the total mass equals 1% of the central star mass, the turbulence is characterized by $\alpha = 0.01$ (Shakura & Sunyaev 1973), the fragmentation velocity is 3 m s^{-1}, and the grain porosity is constant at 30%. The code calculates the radial profile of the mass-dominating grain size and the dust surface density, which is then integrated to obtain the total millimeter flux as a function of time.

Figure 9 shows the evolution of the millimeter flux around two stars, one having a mass equal to 0.2 $M_\odot$ (y-axis) and the other 2 $M_\odot$ (x-axis). In the left panel the dust disk temperature is assumed to be fixed to 20 K, while in the right panel it varies radially and equals the gas disk temperature, which is prescribed to decrease with radius and be higher around high-mass stars: $T_{gas} = 280$ K $\times (r/\mathrm{au})^{-0.5}(M_*/M_\odot)^{0.5}$. While the resulting millimeter fluxes depend on the assumed dust disk

temperature, as highlighted in Section 5, the evolutionary behavior is the same. More specifically, growth and fragmentation (red dashed line and symbols) do not change the initial flux ratio of the two disks and hence cannot explain the steepening of the M_{dust}–M_* relation with time. Growth and drift (light-blue dot-dashed line and symbols) are faster in denser disks around higher-mass stars; hence, these disks are depleted faster of millimeter grains and become millimeter faint sooner than disks around lower-mass stars. This is opposite to what is observed. Finally, the more realistic case of growth, radial drift, and fragmentation (black dotted line and symbols) shows a behavior consistent with the observations, in that the disk around the 0.2 $M_\odot$ star reduces its millimeter flux faster than the disk around the 2 $M_\odot$ star. This is because the timescale on which radial drift removes the largest grains is shorter around low-mass stars. As a result, the disk around the 2 $M_\odot$ star can remain millimeter bright longer. To first order the timescale over which dust is removed is the inverse of the Stokes number (St) of the largest grains, which, in the Epstein regime, scales as St$^{-1} \propto \alpha (c_s/v_{frag})^2 \propto (M_*)^{0.5}$ in the fragmentation-limited case and as St$^{-1} \propto (c_s/v_K)^2 \propto (M_*)^{-0.5}$ in the drift-limited case (Birnstiel et al. 2012). Thus, dust removal is faster around lower-mass stars only in the fragmentation-limited case. For the specific models shown in Figure 9, the maximum grain size is <0.1 mm outside of ~50 au around the 2 $M_\odot$ star and outside of ~15 au around the 0.2 $M_\odot$ star.

In summary, the comparison between models and observations suggests that the maximum grain size in the outer disk is fragmentation limited, rather than drift limited. As already pointed out in the literature (e.g., Pinilla et al. 2013), a reduced

drift efficiency, perhaps caused by radial pressure bumps, is necessary in all models to match the observed lifetime of disks at millimeter wavelengths.

The scenarios discussed above can be tested with future millimeter observations. If grain growth from millimeter to centimeter in size is responsible for the steepening of the $M_{\rm dust}-M_*$ relation with time (Barenfeld et al. 2016), we should expect a stellar-mass- and time-dependent power-law index β of the dust opacity. More specifically, older disks around lower-mass stars should have a lower β than disks around younger, higher-mass stars. A dependence of β with stellar mass is not seen for Taurus disks around ~0.4–2.2 $M_\odot$ stars and for a few disks around substellar objects (Ricci et al. 2010, 2014), but it should be tested if it arises over a statistically significant sample of disks spanning a broad range in stellar masses and at later evolutionary times. If instead the maximum grain size is fragmentation limited as we suggest, the β dependence with stellar mass would be opposite because higher-mass stars would have, on average, larger grains in their disks than lower-mass stars. In addition, there would not be a time dependence because the fragmentation-limited regime is insensitive to the surface density evolution (Birnstiel et al. 2012).

Another prediction of this scenario is that disks around lower-mass stars would be smaller in size than disks around higher-mass stars. Previous work has pointed out that dust disk radii correlate positively with millimeter fluxes for T Tauri stars (Isella et al. 2009; Andrews et al. 2010; Guilloteau et al. 2011), but the scatter is large and what is really needed is to demonstrate a correlation with stellar mass. In the substellar regime, there are only five disks whose dust disk radii at millimeter wavelengths can be reliably inferred. The three in Taurus are rather large (50–100 au; Ricci et al. 2014), while the two in ρ Oph are much smaller (<25 au; Testi et al. 2016). A systematic ALMA survey with high spatial resolution and sufficient S/N is missing.

Finally, we would like to comment on the finding of a longer disk lifetime around low-mass stars based on infrared observations. Carpenter et al. (2006) found that the fraction of optically thick disks in Upper Sco is higher for K+M dwarfs (~0.1–1 $M_\odot$) than for earlier spectral type stars. Expanding on this, Bayo et al. (2012) reported a higher fraction of optical thick disks around stars less massive than ~0.6 $M_\odot$ in the 5–12 Myr old Collinder 69 cluster. These results demonstrate that the inner disk of low-mass stars is not depleted of micron-sized grains, but they do not place any constraint on the outer disk. On the contrary, the ALMA observations presented in this paper trace the population of millimeter grains in the outer disk. Inward-drifting millimeter grains that collide and replenish the inner disk of smaller submicron grains might explain both the apparent lack of millimeter grains in the outer disk and the longer-lived optically thick disks around low-mass stars.

6.3. The Mass Accretion Rate–Disk Mass Relation

In the classical paradigm of disk evolution, the accretion of disk gas onto the star is thought to result from the coupling of the stellar magnetic field with ions in so-called active layers of the disk (magnetorotational instability model; e.g., Gammie 1996). However, in this standard picture the accretion rate is independent from the mass of the central star. Hartmann et al. (2006) showed that a weak linear dependence can be recovered when including stellar irradiation as a disk-heating mechanism

in addition to viscous accretion. Further steepening the relation would be possible if disks around very low mass stars are less massive, are fully magnetically active, and as such have viscously evolved substantially (Hartmann et al. 2006). Alternatively, Ercolano et al. (2014) have proposed that the $\dot{M}-M_*$ relation is flatter for spectral types earlier than M due to a specific disk dispersal mechanism, star-driven X-ray photo-evaporation. Looking at the complete stellar mass range, Dullemond et al. (2006) have shown that a steep $\dot{M} \sim (M_*)^{1.8}$ relation arises naturally if the centrifugal radius of the parent core is independent of the mass of the core, and the spread in $\dot{M}$ at any stellar mass would reflect an initial distribution of core rotation rates. In all cases, $\dot{M}$ should scale linearly with the disk mass, implying that the $\dot{M}-M_*$ relation should be the same as the disk mass–stellar mass relation.

The $\dot{M}-M_*$ relation has been determined for Taurus, Lupus, and Chamaeleon I, while it is not available for Upper Sco. For these three young regions the relation is close to a power law of two: $\dot{M} \propto (M_*)^{1.9\pm0.3}$ for Taurus (Herczeg & Hillenbrand 2008), $\dot{M} \propto (M_*)^{1.8\pm0.2}$ for Lupus (Alcalá et al. 2014), and $\dot{M} \propto (M_*)^{1.7\pm0.4}$ for Chamaeleon I (Manara et al. 2016a). While we do not have total (gas+dust) disk masses, it is interesting to note that $M_{\rm dust}$ displays the same steep relation with M_* in these three regions if the average dust temperature is constant, while the relation is slightly shallower for a dust temperature scaling with stellar luminosity (see Table 4). A more robust way to test the basic prediction of a linear relation between $\dot{M}$ and disk mass is to directly relate these quantities for the same large sample of objects belonging to the same star-forming region. This could be recently achieved for the Lupus clouds. Assuming a constant dust temperature to convert millimeter fluxes into dust disk masses, Manara et al. (2016b) showed that $\dot{M}$ and $M_{\rm dust}$ are correlated in Lupus in a way that is compatible with viscous evolution models. Interestingly, the gas disk mass inferred from CO isotopologues does not show a similar correlation with $\dot{M}$. This may be the result of CO not being a good tracer of the total gas disk mass because carbon can be sequestered in more complex molecules on icy grains (e.g., Bergin et al. 2014) and/or because of complex isotope-selective processes (Miotello et al. 2014, 2016). It would be interesting to extend such studies to other regions, especially Upper Sco, where the $M_{\rm dust}-M_*$ relation is even steeper than in younger star-forming regions.

6.4. Total Disk Masses and Planetary Systems

Given the relevance of disk masses to planet formation models, we discuss here the uncertainties in estimating total disk masses, whether disks appear to be close to being gravitationally unstable, and how dust disk masses compare to the amount of solids locked into exoplanets.

As discussed in Section 5, the average disk temperature tracing millimeter emission affects the absolute value of the dust disk mass, as well as the disk–stellar mass scaling relation, with cooler temperatures leading to higher disk mass estimates. For the two temperature relations adopted here the average difference in dust disk masses amounts to a factor of ~3. An even larger uncertainty is introduced by the dust opacity, which depends on grain composition and size distribution (see, e.g., Testi et al. 2014), which are both still poorly constrained. Silicates constitute the main source of opacity at ~1 mm. While plausible uncertainties in their optical constants affect the dust opacity by no more than a factor of two, porosity adds an
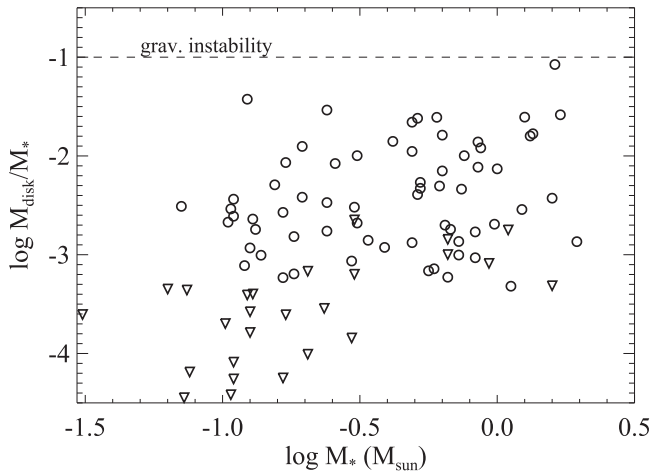
Figure 10. Disk-to-stellar mass ratios as a function of stellar masses (M_*) for our Chamaeleon I region. Disk masses are dust masses (using a constant dust disk temperature of 20 K) multiplied by 100.
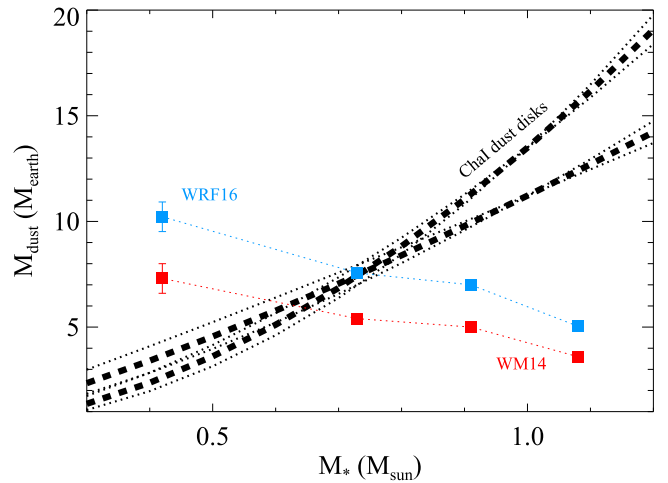

Figure 11. Dust disk masses in Chamaeleon I (black dashed and dotted lines) compared to the average mass in solids (red and blue squares) from the *Kepler* exoplanets as computed in Mulders et al. (2015b). The planet mass–radius relation by WRF16 (Wolfgang et al. 2016) gives a higher average mass than that by WM14 (Weiss & Marcy 2014). Regardless of the assumed relation, low-mass stars (∼0.4 $M_\odot$) have dust disk masses lower than the average mass locked up in close-in exoplanets.

uncertainty of a factor of several for grains larger than 100 μm (Pollack et al. 1994; Henning & Stognienko 1996; Semenov et al. 2003). Even assuming a fixed dust composition, the 1.3 mm opacity can vary by a factor of ∼4 depending on whether the grain size distribution extends to 1 cm (low opacity = higher mass) or to 0.8 mm (high opacity = lower mass); see, e.g., Figure 1 in Tazzari et al. (2016). The 2.3 cm^2 g^{-1} dust opacity we have adopted is close to the one for a grain size distribution extending to 1 cm. This means that if the true grain size distribution were truncated at 1 mm, the dust disk masses would be a factor of 4 lower than those we report. Given that our choice of dust opacity maximizes dust disk masses over the range of grain sizes expected/detectable in the outer disk, we will continue our discussion adopting the dust disk masses obtained with a constant dust temperature, which, instead, minimizes the disk masses toward lower-mass stars.

Figure 10 shows the distribution of M_{disk}/M_*, where M_{disk} is simply the dust disk mass multiplied by the interstellar medium (ISM) gas-to-dust ratio of 100. Although recent gas mass estimates using rotational lines from CO isotopologues have claimed gas-to-dust ratios well below the ISM value in young disks (Williams & Best 2014; Ansdell et al. 2016), detailed physico-chemical disk models need to be carried out to properly account for isotope-selective processes (Miotello et al. 2014, 2016). In addition, carbon can be extracted from CO via reactions with He$^+$ and form hydrocarbons that freeze out, thus reducing the CO abundance in the disk atmosphere (Favre et al. 2013). Indeed, the only disk with an independent mass estimate, using the HD ($J = 1-0$) transition at far-infrared wavelengths, has a gas-to-dust mass ratio consistent with the ISM value and confirms that masses using CO isotopologues can be off by up to a factor of 100 (Bergin et al. 2013). With these caveats, it is interesting to compare the inferred distribution of M_{disk}/M_* ratios to the limiting mass ratio above which gravitational instabilities set in ($M_{disk}/M_* \sim 0.1$; e.g., Lodato et al. 2005; dashed line in Figure 10). While the median M_{disk}/M_* value of ∼0.04 is well below 0.1, the brightest source in our sample is close to the gravitational instability boundary. In addition, six other sources, ranging in stellar mass from ∼0.15 to 1.7 $M_\odot$, have ratios only a factor of 4 lower than the gravitational instability limit and appear to

delineate an upper horizontal boundary. It is interesting to speculate that this upper boundary is the one set by gravitational instability, but independent observations of the gas content are necessary to make any firm conclusion.

How do disk masses compare with the mass locked up in exoplanets around other stars? Najita & Kenyon (2014) used a Monte Carlo approach to create ensembles of systems with planets and debris disks at their known incidence rates and compared them to the Taurus protoplanetary disk masses from Andrews et al. (2013). They found that the mass in solids in Class II sources is barely enough to account for the known population of *Kepler* and RV planets plus debris disks and seems to fall short for the 5–30 $M_\oplus$ planets at 0.5–10 au discovered by microlensing. Mulders et al. (2015b) focused on stellar mass dependencies in the amount of solids from the well-characterized *Kepler* survey, probing planets with periods within 50 days (∼0.3 au around a solar-mass star). They pointed out that the average mass in solids locked up in exoplanets increases roughly inversely with stellar mass instead of decreasing as the dust disk mass estimated from millimeter observations. Figure 11 compares dust disk masses in Chamaeleon I with the solid mass in exoplanets. For solar- or higher-mass stars dust disk masses are larger than the mass of solids locked up in close-in exoplanets. However, ∼2 Myr old disks around low-mass stars (∼0.4 $M_\odot$) appear to be already short in solids by a factor of at least 2 to reproduce the average mass in exoplanets. At ∼10 Myr the deficit amounts to more than a factor of 5 as shown by the Upper Sco region. Recently, Gillon et al. (2016) reported the discovery of three close-in (<0.1 au) Earth-size planets around the 0.08 $M_\odot$ star TRAP-PIST-1. Interestingly, the largest dust disk mass that we can obtain from the relations in Table 4 for such a star is only 1.6 $M_\oplus$, not enough to reproduce the total mass in the TRAPPIST-1 planetary system. Even if half of the disk mass is already converted into planetesimals in ∼1 Myr old disks as proposed by Najita & Kenyon (2014), dust disk masses around low-mass stars are still on the low side to account for the solid mass in close-in exoplanets. As discussed in Section 6.1, inward drift most likely contributes to redistribute the mass of

millimeter grains early on. If so, there should be a large population of millimeter grains closer in to the star at radii that our observations are not sensitive to. It is unclear whether such grains will retain their size for long or quickly grow to form the close-in planets we see around mature stars.

7. CONCLUSIONS

We presented an ALMA $887\,\mu$m survey of the disk population around objects from $\sim$2 to $0.03\,M_\odot$ in the nearby $\sim$2 Myr old Chamaeleon I star-forming region. One of our main goals was to use the continuum emission to estimate dust disk masses and establish how they scale with stellar mass. Our main findings can be summarized as follows:

1. We detect thermal dust emission from 66 out of 93 disks, spatially resolve 34 of them, and identify two disks with large dust cavities ($\sim$45 au in radius).
2. We find that the disk–stellar mass scaling relation in Chamaeleon I is steeper than linear: $M_{\rm dust} \propto (M_*)^{1.3–1.9}$, where the range in the power-law index reflects two extreme relations between the average dust temperature and stellar luminosity.
3. By reanalyzing in a self-consistent way all millimeter data available for nearby regions, we show that the 1–3 Myr old regions of Taurus, Lupus, and Chamaeleon I have the same $M_{\rm dust}$–M_* relation, while the 10 Myr old Upper Sco association has an even steeper relation.
4. The dispersion around the $M_{\rm dust}$–M_* relation is very similar among regions with ages $\sim$1–10 Myr, hinting at a range of initial conditions that might partly account for the diversity of planetary systems.
5. The slopes of the $M_{\rm dust}$–M_* and the $\dot{M}$–M_* relations are the same for Taurus, Chamaeleon I, and Lupus when assuming a constant dust temperature, in agreement with the basic expectation from viscous disk models.

By comparing our results with theoretical models of grain growth, drift, and fragmentation, we show that a steeping of the $M_{\rm dust}$–M_* relation with time occurs if outer disks are in the fragmentation-limited regime. This is because when fragmentation sets the largest grain size, radial drift will occur at shorter timescales around lower-mass stars. This scenario of redistributing mass in the disk can also account for the apparent lack of solids in million-year-old disks around low-mass stars ($\leqslant 0.4\,M_\odot$) when compared to the average mass of solids locked into close-in exoplanets. Such a scenario results in a stellar-mass-dependent but not a time-dependent power-law index of the dust opacity. It also implies a stellar-mass-dependent disk size for millimeter grains. Deeper and higher-resolution millimeter observations are needed to test the predicted trends. Establishing whether and how the size of dust disks scales with stellar mass will also enable us to measure the dependence between the average dust temperature and stellar luminosity, which is crucial for pinning down the exact $M_{\rm dust}$–M_* relation.

Table 5
Summary of Methods for the $F_{\rm mm}$−M_* Relation in Chamaeleon I

Routine	Method	Censored	Slope	Intercept
fitexy (IDL)	Nukers	n	2.43(0.08)	2.16(0.04)
mpfitexy (IDL)	Nukers (with scatter)	n	1.5(0.2)	1.8(0.1)
censReg (R)	Maximum likelihood	y	1.8(0.2)	1.6(0.1)
cenken (R)	Akritas-Thiel-Sen	y	1.9	1.7
linmix_err (IDL)	Bayesian	y	1.9(0.2)	1.6(0.1)

Note. Uncertainties in the slope and intercept are reported in parentheses.

APPENDIX
COMPARISON OF LINEAR REGRESSION METHODS

Here we compare different linear regression methods to fit the $F_{\rm mm}$−M_* relation in the log–log plane. We will show how the intrinsic scatter in the relation and censored values (upper limits to the millimeter flux density) contribute to the best-fit slope and intercept.

We start by comparing the results from two IDL routines (fitexy and mpfitexy) that do not account for upper limits, i.e., we only fit the 66 sources with measured flux densities. Both routines assume symmetric measurement errors in x [$\log(M_*)$] and y [$\log(F_{\rm mm})$] and use the Nukers estimator to find the best fit (see, e.g., Tremaine et al. 2002). The main difference is that mpfitexy accounts for the intrinsic scatter and can automatically adjust it to ensure a reduced χ^2 of unity. Indeed, this is necessary for our data set, where $F_{\rm mm}$ has a large spread at each stellar mass, and confirmed by the fact that fitexy cannot find a good fit, the χ^2 is greater than 550 and the probability that the model is correct is zero. The mpfitexy requires a scatter about the relation of 0.5 dex to obtain

$\chi^2 \sim 1$. In addition, the uncertainties in the slope and intercept from fitexy are unrealistically low, and the best fit is dominated by a few precise measurements when not accounting for the scatter, thus biasing the derived slope and intercept (see Table 5). These issues are well documented in Tremaine et al. (2002).

Next, we compare three different routines that account for censored data using different methods. The one utilized throughout the paper is the linmix_err routine (IDL version) written by Kelly (2007) and already used in several other astronomical applications. This routine accounts for both measurement errors and intrinsic scatter, while the other two routines from the R statistical package (censReg and cenken) do not include individual measurement errors. The fact that they all provide the same slope and intercept within the quoted uncertainties (Table 5) again confirms that the intrinsic scatter about the relation drives the best fit. In what follows we briefly summarize the methods used in these routines and additional lessons learned from the comparison.

The linmix_err routine uses a Bayesian approach assuming a normal linear regression model, i.e., the conditional distribution is a normal density, and computes the likelihood function of the data by integrating the conditional distribution. The measurement errors and the intrinsic scatter about the line are all assumed to be normally distributed. A Markov chain Monte Carlo method is used to compute the uncertainties on the slope and intercept. Further details about the approach are summarized in Kelly (2007).

The censReg R routine is based on the parametric maximum likelihood estimation and assumes a normal distribution of the error term (see, e.g., Greene 2008). As mentioned above, individual measurement errors on x and y are not taken into account, and one single left censoring (upper limit) is considered. Because our survey has different upper limits for the *Hot* and *Cool* samples, we had to use the less stringent one, the one from the *Hot* sample. In other words, the results reported in Table 5 are from treating 58 data points as uncensored (detections) and 35 as upper limits; 27 of them are true upper limits, while 8 are additional detections below the upper limit set by the *Hot* sample.

Finally, the cenken R routine uses the nonparametric Akritas–Thiel–Sen line with the Turnbull estimate of intercept (Akritas et al. 1995). The advantage of this method is that it does not make any assumption about the distribution of the data. While measurement errors on x and y are not included, upper limits can be specified individually, meaning that both the *Hot* and *Cool* sample upper limits can be properly taken into account.

As summarized in Table 5, the three routines treating censored data find the same slope and intercept for the F_{mm}–M_* relation. As expected, the slope is steeper and the intercept is lower than that obtained considering only uncensored data but properly accounting for the scatter (mpfitexy). The slightly lower slope from censReg probably reflects that the *Cool* sample upper limits are not treated (see also Section 4 for a similar effect when applying an even shallower cutoff as in the Taurus survey). Finally, the fact that parametric and nonparametric approaches reach the same results suggests that the slope and intercept of the F_{mm}–M_* relation are not affected by the underlining assumptions on the distribution of the data.

REFERENCES

Akritas, M. G., Murphy, S. A., & LaValley, M. P. 1995, J. Am. Stat. Assoc., 90, 170

Alcalá, J. M., Natta, A., & Manara, C. F. 2014, A&A, 561, A2

Alexander, R., Pascucci, I., Andrews, S., Armitage, P., & Cieza, L. 2014, in Protostars and Planets VI, ed. H. Beuther et al. (Tucson, AZ: Univ. Arizona Press), 475

Alexander, R. D., & Armitage, P. J. 2006, ApJL, 639, L83

Alibert, Y., Mordasini, C., & Benz, W. 2011, A&A, 526A, 63

Andrews, S. M., Rosenfeld, K. A., Kraus, A. L., & Wilner, D. J. 2013, ApJ, 771, 129

Andrews, S. M., Wilner, D. J., Hughes, A. M., Qi, C., & Dullemond, C. P. 2010, ApJ, 723, 1241

Ansdell, M., Williams, J. P., van der Marel, N., et al. 2016, ApJ, 828, 46

Anthonioz, F., Ménard, F., Pinte, C., et al. 2015, A&A, 574, A41

Baraffe, I., Chabrier, G., Allard, F., & Hauschildt, P. H. 1998, A&A, 337, 403

Baraffe, I., Homeier, D., Allard, F., & Chabrier, G. 2015, A&A, 577, A42

Barenfeld, S., Carpenter, J. M., Ricci, L., & Isella, A. 2016, ApJ, 827, 142

Bayo, A., Barrado, D., Huelamo, N., et al. 2012, A&A, 547, A80

Beckwith, S. V. W., Henning, T., & Nakagawa, Y. 2000, in Protostars and Planets IV, ed. V. Mannings, A. P. Boss, & S. S. Russell (Tucson, AZ: Univ. Arizona Press), 533

Beckwith, S. V. W., Sargent, A. I., Chini, S., & Guesten, R. 1990, AJ, 99, 924

Belloche, A., Schuller, F., Parise, B., et al. 2011, A&A, 527, A145

Bergin, E. A., Cleeves, L. I., Crockett, N., & Blake, G. A. 2014, FaDi, 168, 61

Bergin, E. A., Cleeves, L. I., Gorti, U., et al. 2013, Natur, 493, 644

Birnstiel, T., Klahr, H., & Ercolano, B. 2012, A&A, 539, A148

Bonfils, X., Delfosse, X., Udry, S., et al. 2013, A&A, 549, A109

Carpenter, J. M., Mamajek, E. E., Hillenbrand, L. A., & Meyer, M. R. 2006, ApJL, 651, L49

Carpenter, J. M., Ricci, L., & Isella, A. 2014, ApJ, 787, 42

Comerón, F. 2008, in Handbook of Star Forming Regions, Volume II: The Southern Sky ASP Monograph Publications, Vol. 5, ed. B. Reipurth (San Francisco, CA: ASP), 295

Cutri, R. M., et al. 2012, yCat, 2311, 0

Daemgen, S., Petr-Gotzens, M. G., Correia, S., et al. 2013, A&A, 554, A43

Dressing, C. D., & Charbonneau, D. 2013, ApJ, 767, 95

Dullemond, C. P., Natta, A., & Testi, L. 2006, ApJL, 645, L69

Eisner, J. A., Bally, J. M., Ginsburg, A., & Sheehan, P. D. 2016, ApJ, 826, 16

Ercolano, B., Mayr, D., Owen, J. E., Rosotti, G., & Manara, C. F. 2014, MNRAS, 439, 256

Espaillat, C., Muzerolle, J., Najita, J., et al. 2014, in Protostars and Planets VI, ed. H. Beuther et al. (Tucson, AZ: Univ. Arizona Press), 497

Fang, M., van Boekel, R., Wang, W., et al. 2009, A&A, 504, 461

Favre, C., Cleeves, L. I., Bergin, E. A., Qi, C., & Blake, G. A. 2013, ApJL, 776, L38

Feiden, G. A. 2016, A&A, 593, A99

Gammie, C. F. 1996, ApJ, 457, 355

Ghez, A. M., McCarthy, D. W., Patience, J. L., & Beck, T. L. 1997, ApJ, 481, 378

Gillon, M., Jehin, E., Lederer, S. M., et al. 2016, Natur, 533, 221

Greene, W. H. 2008, Econometric Analysis (6th ed.; Englewood Cliffs, NJ: Prentice-Hall)

Guilloteau, S., Dutrey, A., Piétu, V., & Boehler, Y. 2011, A&A, 529, A105

Guilloteau, S., Piétu, V., Chapillon, E., et al. 2016, A&A, 586, L1

Harris, R. J., Andrews, S. M., Wilner, D. J., & Kraus, A. L. 2012, ApJ, 751, 115

Hartmann, L., D'Alessio, P., Calvet, N., & Muzerolle, J. 2006, ApJ, 648, 484

Harvey, P. M., Henning, Th., Liu, Y., et al. 2012, ApJ, 755, 67

Henning, T., Pfau, W., Zinnecker, H., & Prusti, T. 1993, A&A, 276, 129

Henning, Th., & Stognienko, R. 1996, A&A, 311, 291

Herczeg, G. J., & Hillenbrand, L. A. 2008, ApJ, 681, 594

Herczeg, G. J., & Hillenbrand, L. A. 2015, ApJ, 808, 23

Howard, A. W., Marcy, G. W., Bryson, S., et al. 2012, ApJS, 201, 15

Hughes, A. M., Wilner, D. J., Calvet, N., et al. 2007, ApJ, 664, 536

Isella, A., Carpenter, J. M., & Sargent, A. I. 2009, ApJ, 701, 260

Johnson, J. A., Aller, K. M., Howard, A. W., & Crepp, J. R. 2010, PASP, 122, 905

Kamp, I., Woitke, P., Pinte, C., et al. 2011, A&A, 532, A85

Kelly, B. C. 2007, ApJ, 665, 1489

Kim, K. H., Watson, D. M., Manoj, P., et al. 2009, ApJ, 700, 1017

Klein, R., Apai, D., Pascucci, I., Henning, Th., & Waters, L. B. F. M. 2003, ApJL, 593, L57

Kraus, A. L., Ireland, M. J., Hillenbrand, L. A., & Martinache, F. 2012, ApJ, 745, 19

Krijt, S., Ormel, C. W., Dominik, C., & Tielens, A. G. G. M. 2016, A&A, 586, A20
Lodato, G., Delgado-Donate, E., & Clarke, C. J. 2005, MNRAS, 364, L91
Luhman, K. L. 2004, ApJ, 617, 1216
Luhman, K. L. 2007, ApJS, 173, 104
Luhman, K. L. 2008, in Handbook of Star Forming Regions, Volume II: The Southern Sky ASP Monograph Publications, Vol. 5, ed. B. Reipurth (San Francisco, CA: ASP), 169
Luhman, K. L., Allen, L. E., Allen, P. R., et al. 2008, ApJ, 675, 1375
Manara, C. F., Fedele, D., Herczeg, G. J., & Teixeira, P. S. 2016a, A&A, 585, A136
Manara, C. F., Rosotti, G., Testi, L., et al. 2016b, A&A, 591, L3
Manara, C. F., Testi, L., Natta, A., et al. 2014, A&A, 568, A18
Manoj, P., Kim, K. H., Furlan, E., et al. 2011, ApJS, 193, 11
Mathis, J. S. 1990, ARA&A, 28, 37
Mathis, J. S., Mezger, P. G., & Panagia, N. 1983, A&A, 128, 212
Miotello, A., Bruderer, S., & van Dishoeck, E. F. 2014, A&A, 572, A96
Miotello, A., van Dishoeck, E. F., Kama, M., & Bruderer, S. 2016, A&A, 594, A85
Mohanty, S., Greaves, J., Mortlock, D., et al. 2013, ApJ, 773, 168
Moór, A., Henning, Th., Juhász, A., et al. 2015, ApJ, 814, 42
Mordasini, C., Alibert, Y., Benz, W., Klahr, H., & Henning, T. 2012, A&A, 541, A97
Mulders, G. D., & Dominik, C. 2012, A&A, 539, A9
Mulders, G. D., Pascucci, I., & Apai, D. 2015a, ApJ, 798, 112
Mulders, G. D., Pascucci, I., & Apai, D. 2015b, ApJ, 814, 130
Najita, J. R., & Kenyon, S. J. 2014, MNRAS, 445, 3315
Natta, A., Grinin, V., & Mannings, V. 2000, Protostars and Planets IV (Tucson, AZ: Univ. Arizona Press)
Natta, A., Testi, L., & Randich, S. 2006, A&A, 452, 245
Obermeier, C., Koppenhoefer, J., Saglia, R. P., et al. 2016, A&A, 587, A49
Olofsson, J., Szűcs, L., Henning, Th., et al. 2013, A&A, 560, A100

Pascucci, I., Apai, D., Luhman, K., et al. 2009, ApJ, 696, 143
Pascucci, I., Gorti, U., Hollenbach, D., et al. 2006, ApJ, 651, 1177
Pascucci, I., Herczeg, G., Carr, J. S., & Bruderer, S. 2013, ApJ, 779, 178
Pecaut, M. J., Mamajek, E. E., & Bubar, E. J. 2012, ApJ, 746, 154
Pinilla, P., Birnstiel, T., Benisty, M., et al. 2013, A&A, 554, A95
Pollack, J. B., Hollenbach, D., Beckwith, S., et al. 1994, ApJ, 421, 615
Raymond, S. N., Scalo, J., & Meadows, V. S. 2007, ApJ, 669, 606
Ribas, A., Merin, B., Bouy, H., & Maud, L. T. 2014, A&A, 561, A54
Ricci, L., Testi, L., Natta, A., et al. 2010, A&A, 512, A15
Ricci, L., Testi, L., Natta, A., et al. 2014, ApJ, 791, 20
Rigliaco, E., Natta, A., Randich, S., Testi, L., & Biazzo, K. 2011, A&A, 525, A47
Robberto, M., Spina, L., Da Rio, N., et al. 2012, AJ, 144, 83
Scholz, A., Jayawardhana, R., & Wood, K. 2006, ApJ, 645, 1498
Semenov, D., Henning, Th., Helling, Ch., Ilgner, M., & Sedlmayr, E. 2003, A&A, 410, 611
Shakura, N. I., & Sunyaev, R. A. 1973, A&A, 24, 337
Siess, L., Dufour, E., & Forestini, M. 2000, A&A, 358, 593
Slesnick, C. L., Hillenbrand, L. A., & Carpenter, J. M. 2008, ApJ, 688, 377
Szűcs, L., Apai, D., Pascucci, I., & Dullemond, C. 2010, ApJ, 720, 1668
Tazzari, M., Testi, L., Ercolano, B., et al. 2016, A&A, 588, A53
Testi, L., Birnstiel, T., Ricci, L., et al. 2014, in Protostars and Planets VI, ed. H. Beuther et al. (Tucson, AZ: Univ. Arizona Press), 339
Testi, L., Nata, A., Scholz, A., et al. 2016, A&A, 593, A111
Tremaine, S., Gebhardt, K., Bender, R., et al. 2002, ApJ, 574, 740
van der Plas, G., Ménard, F., Ward-Duong, K., et al. 2016, ApJ, 819, 102
Weiss, L. M., & Marcy, G. W. 2014, ApJL, 783, L6
Williams, J. P., & Best, W. M. J. 2014, ApJ, 788, 59
Williams, J. P., & Cieza, L. A. 2011, ARA&A, 49, 67
Winn, J. N., & Fabrycky, D. C. 2015, ARA&A, 53, 409
Wolfgang, A., Rogers, L. A., & Ford, E. B. 2016, ApJ, 825, 19